Original Research Article | Open Access

The Journal of Cardiovascular Aging

Jia et al. J Cardiovasc Aging. 2026;6:45 DOI:10.20517/jca.2026.81

Lnc-mg regulates cardiomyocyte contraction and promotes functional recovery after ischemic injury

Songrui Jia[1,#], Yang Cui[1,#], Mengge Wu[4], Chenghao Fan[1], Yu Nie[1,2], Yanhai Meng[1,3], Lina Bai[1]

Keywords:
Long non-coding RNA, myocardial infarction, myocardial contractility, cardiac function

Citation: Jia S, Cui Y, Wu M, Fan C, Nie Y, Meng Y, Bai L. *Lnc-mg* regulates cardiomyocyte contraction and promotes functional recovery after ischemic injury. *J Cardiovasc Aging.* 2026;6:45. https://dx.doi.org/10.20517/jca.2026.81

Received: 28 Jun 2026
First Decision: 24 Jul 2026
Revised: 28 Aug 2026
Accepted: 1 Sep 2026
Published: 16 Sep 2026

Academic Editor: Xiaoqiang Tang
Copy Editor: Fangling Lan
Production Editor: Fangling Lan

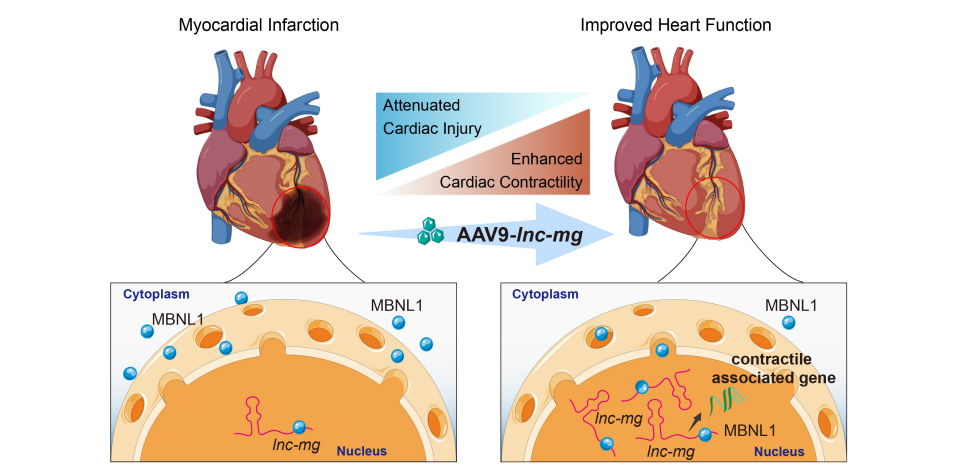

Abstract

Aim: Persistent loss of cardiomyocyte contractile function is a major driver of cardiac dysfunction following myocardial infarction (MI). Long noncoding RNAs (lncRNAs) have emerged as important regulators of cardiac biology, yet their contribution to maintenance of myocardial contractility remains incompletely understood. To address this question, we investigated the role of the muscle-enriched lncRNA *lnc-mg* in cardiomyocyte contractility and its underlying molecular basis.

Methods: Ardiomyocyte-specific *lnc-mg* knockout mice were generated to investigate the physiological function of *lnc-mg* in the heart. Cardiac function, exercise capacity,

[1]State Key Laboratory of Cardiovascular Disease, Fuwai Hospital, Chinese Academy of Medical Sciences and Peking Union Medical College, Beijing 100037, China.
[2]Fuwai Yunnan Hospital, Chinese Academy of Medical Sciences, Affiliated Cardiovascular Hospital of Kunming Medical University, Kunming 650102, Yunnan, China.
[3]Department of Surgical Intensive Care Unit, Fuwai Hospital, National Center for Cardiovascular Diseases, Chinese Academy of Medical Sciences and Peking Union Medical College, Beijing 100037, China.
[4]Experimental Animal Center, Central China Subcenter of National Center for Cardiovascular Diseases, Henan Cardiovascular Disease Center, Zhengzhou 450046, Henan, China.
[#]The authors contributed equally and are co-first authors.

Correspondence to: Dr. Yu Nie, State Key Laboratory of Cardiovascular Disease, Fuwai Hospital, Chinese Academy of Medical Sciences and Peking Union Medical College, 167 Beilishi Road, Xicheng District, Beijing 100037, China; Fuwai Yunnan Hospital, Chinese Academy of Medical Sciences, Affiliated Cardiovascular Hospital of Kunming Medical University, Kunming 650102, Yunnan, China. E-mail: nieyuniverse@126.com; Dr. Yanhai Meng, State Key Laboratory of Cardiovascular Disease, Fuwai Hospital, Chinese Academy of Medical Sciences and Peking Union Medical College, 167 Beilishi Road, Xicheng District, Beijing 100037, China; Department of Surgical Intensive Care Unit, Fuwai Hospital, National Center for Cardiovascular Diseases, Chinese Academy of Medical Sciences and Peking Union Medical College, Beijing 100037, China. E-mail: mengyanhai@126.com; Dr. Lina Bai, State Key Laboratory of Cardiovascular Disease, Fuwai

Hospital, Chinese Academy of Medical Sciences and Peking Union Medical College, 167 Beilishi Road, Xicheng District, Beijing 100037, China. E-mail: bailina0520@163.com

myocardial tissue contractility, and single-cardiomyocyte contractility were assessed by echocardiography, treadmill testing, the Myostation-intact system, and the IonOptix platform, respectively. RNA-seq of myocardial tissue, bioinformatic prediction, RNA immunoprecipitation, molecular docking, immunofluorescence, and analysis of published cardiac MBNL1 CLIP-seq data were used to investigate the underlying molecular mechanism. Finally, Adeno-associated virus 9 (AAV9)-mediated overexpression of *lnc-mg* in cardiomyocytes was evaluated in a mouse model of MI.

Results: *Lnc-mg* was highly enriched in cardiomyocytes and progressively increased during postnatal cardiac development. Cardiomyocyte-specific deletion of *lnc-mg* impaired left ventricular systolic function, exercise capacity, and contractility at both the myocardial tissue and single-cardiomyocyte levels. Consistent with these functional abnormalities, *lnc-mg* deficiency was accompanied by coordinated suppression of gene programs governing sarcomere organization, myofibril assembly, actomyosin organization, and muscle contraction. MBNL1 was identified as an *lnc-mg*-associated RNA-binding protein. The nuclear localization of MBNL1 was reduced following *lnc-mg* deficiency, and MBNL1-bound cardiac transcripts are enriched for cardiomyocyte contractile gene programs. Importantly, AAV9-mediated *lnc-mg* overexpression in cardiomyocytes preserved cardiac systolic function, attenuated chronic fibrotic remodeling, and improved myocardial tissue contractility after MI.

Conclusion: Our study identifies *lnc-mg* as a previously unrecognized regulator of cardiomyocyte contractile function and suggests that an *lnc-mg*-MBNL1-associated mechanism may contribute to the maintenance of cardiac contractile gene programs. These observations provide a rationale for further investigation of *lnc-mg* as a potential therapeutic target for preserving myocardial contractility after ischemic injury.

INTRODUCTION

Ischemic heart disease remains the leading cause of cardiovascular death worldwide and a major cause of chronic heart failure[1,2]. Myocardial infarction (MI), a major acute manifestation of ischemic heart disease, results from prolonged myocardial ischemia and causes irreversible cardiomyocyte loss[3,4]. Beyond the initial loss of viable myocardium, ischemic injury induces persistent contractile dysfunction in the surviving myocardium, contributing to progressive pump failure and adverse left ventricular remodeling[5-7]. Recent studies in murine models have underscored that restoring cardiomyocyte contractile function can preserve ventricular performance and animal survival after MI[8-10]. However, the endogenous regulators that promote cardiomyocyte contraction remain incompletely defined. Therefore, identifying these regulators remains an important goal for understanding cardiac physiology and developing therapeutic approaches for ischemic heart failure.

Long noncoding RNAs (lncRNAs) are generally defined as transcripts longer than 200 nucleotides with limited or no protein-coding potential[11]. Accumulating evidence indicates that lncRNAs broadly participate in biological processes under physiological and pathological conditions[12]. In the heart, lncRNAs have emerged as important regulators of cardiac homeostasis and responses to stress, including *Mhrt* and *DCRT*[13,14]. In models of MI or ischemia-reperfusion injury, cardioprotective lncRNAs have been shown to limit cardiomyocyte apoptosis, modulate oxidative stress, and regulate cardiac remodeling and functional recovery[15-19]. However, despite growing recognition of their cardioprotective roles, the contribution of lncRNAs to the regulation of myocardial contractility remains incompletely understood.

Lnc-mg (also known as *Myhas*) is a muscle-enriched lncRNA. Genetic deletion of *lnc-mg* in skeletal muscle resulted in reduced tetanic force and impaired exercise endurance, whereas skeletal muscle-specific overexpression promoted muscle hypertrophy and force generation, establishing *lnc-mg* as a positive

regulator of myogenic differentiation, skeletal muscle development, and muscle function[20]. Emerging evidence indicates that some muscle-associated lncRNAs exert regulatory functions in both skeletal and cardiac muscle, supporting that molecular pathways governing skeletal muscle biology may also contribute to cardiac function[21-23]. However, despite the established role of *lnc-mg* in skeletal muscle, its cardiac expression pattern, physiological function, and molecular mechanisms remain unknown.

In the present study, we investigated the role of *lnc-mg* in the heart using cardiomyocyte-specific loss- and gain-of-function approaches. We demonstrate that *lnc-mg* is highly enriched in cardiomyocytes and is required for maintaining normal myocardial contractile function. Conversely, *lnc-mg* overexpression enhances cardiomyocyte contractility and improves cardiac functional recovery following MI. Together, our findings establish *lnc-mg* as a previously unrecognized regulator of myocardial contractility and broaden current understanding of the roles of muscle-associated lncRNAs in cardiac physiology and disease.

MATERIAL AND METHODS

Experimental animals

All animals included in the experimental analyses were male, specific pathogen-free mice. P1 neonatal C57BL/6 mice used for primary neonatal cardiomyocyte isolation and 2-month-old C57BL/6 mice used for MI experiments were purchased from SPF (Beijing) Biotechnology Co., Ltd. (Beijing, China). The age of the mice used in each experiment is specified in the corresponding subsection and figure legend. At 2 months of age, the mice weighed approximately 20-25 g.

Adult mice were housed in the accredited animal facility of Fuwai Hospital at 25 °C and 55%-65% relative humidity under a 12-h light/dark cycle. Standard laboratory chow and water were available ad libitum, and the mice were allowed to acclimatize for at least 7 days before experimentation. P1 neonatal mice were used for cardiomyocyte isolation upon arrival.

All animal experiments were approved by the Institutional Animal Care and Use Committee of Fuwai Hospital, Chinese Academy of Medical Sciences and Peking Union Medical College (approval No. 0108-7-2200-ZX) and were conducted in accordance with the Guide for the Care and Use of Laboratory Animals and institutional guidelines. The researchers performing histological analysis were blinded to the experimental groups. Mice were randomly assigned to different experimental groups.

Generation, genotyping, and validation of cardiomyocyte-specific *lnc-mg* knockout mice

The *lnc-mg*$^{fl/fl}$ mice were generated on a C57BL/6J genetic background using a targeting vector containing 5′ and 3′ homology arms, two loxP sites flanking exon 1 of *lnc-mg*, an FRT-flanked neomycin-resistance cassette for positive selection, and a diphtheria toxin A cassette for negative selection. The targeting construct was introduced into C57BL/6J-derived embryonic stem cells by electroporation, as previously described by Zhu *et al.*[20], and the resulting mice were provided by Dr. Xiaogang Wang's laboratory at Beihang University, Beijing, China. Constitutive cardiomyocyte-specific *cTnT*-Cre transgenic mice [Tg(Tnnt2-cre)5Blh; corresponding to the mixed-background JAX stock No. 024240; RRID: IMSR_JAX:024240], in which an nls-Cre-hGH cassette is driven by the rat *Tnnt2* promoter, were originally generated by Jiao *et al.*[24] and were provided by Professor Bin Zhou's laboratory at the Center for Excellence in Molecular Cell Science, Chinese Academy of Sciences, Shanghai, China.

To generate cardiomyocyte-specific *lnc-mg* knockout mice, *cTnT*-Cre mice were first crossed with *lnc-mg*$^{fl/fl}$ mice. Cre-positive *lnc-mg*$^{fl/+}$ offspring were subsequently bred with *lnc-mg*$^{fl/fl}$ mice to obtain *cTnT*-Cre-positive *lnc-mg*$^{fl/fl}$ mice, hereafter referred to as *lnc-mg* cKO mice. Cre-negative *lnc-mg*$^{fl/fl}$ littermates generated from the same crosses served as controls.

Genomic DNA was isolated from tail biopsies, and the *lnc-mg* floxed allele was identified by genotyping polymerase chain reaction (PCR) using an initial denaturation at 95 °C for 5 min, followed by 35 cycles of denaturation at 95 °C for 30 s, annealing at 62 °C for 30 s, and extension at 72 °C for 20 s, with a final extension at 72 °C for 10 min. The wild-type (WT) and floxed alleles yielded amplicons of 209 and 263 bp, respectively; accordingly, WT mice displayed only the 209-bp product, heterozygous mice displayed both the 209- and 263-bp products, and homozygous floxed mice displayed only the 263-bp product.

The *cTnT*-Cre transgene was detected by genotyping PCR using an initial denaturation at 95 °C for 3 min, followed by 35 cycles of denaturation at 95 °C for 30 s, annealing at 60 °C for 30 s, and extension at 72 °C for 30 s, with a final extension at 72 °C for 10 min. The Cre-specific and internal positive-control (IPC) primer pairs generated amplicons of 528 and 324 bp, respectively. Cre-positive mice displayed both the 528-bp Cre-specific product and the 324-bp IPC product, whereas Cre-negative mice displayed only the 324-bp IPC product. Samples lacking the IPC product were considered technically invalid and were reanalyzed. The corresponding primer sequences are provided in Supplementary Data 1.

Echocardiographic assessment of cardiac function

Mice were anesthetized with 1.5% isoflurane for induction and maintained under 0.5% isoflurane. The animals were placed in the supine position on a heated platform, the chest hair was removed, and ultrasound gel was applied. Transthoracic echocardiography was performed using a Vevo 2100 small-animal ultrasound system equipped with a 30-MHz high-frequency transducer (FUJIFILM VisualSonics). M-mode images were obtained from short-axis views of the left ventricle at the level of the papillary muscles, with clear visualization of the anterior and posterior ventricular walls and the interventricular septum. Left ventricular end-diastolic diameter and end-systolic diameter were measured over at least three consecutive cardiac cycles, and left ventricular ejection fraction (LVEF) and left ventricular fractional shortening (LVFS) were calculated using Vevo analysis software.

Sample sizes for the longitudinal echocardiographic studies were determined by a priori power analyses using G*Power version 3.1[25], with LVEF prespecified as the primary functional endpoint. For the *lnc-mg* cKO study, an anticipated between-group difference of 8 percentage points and a pooled standard deviation of 5 percentage points were used. For the post-infarction study, the corresponding assumptions were 12 and 7.5 percentage points, respectively. With a two-sided α of 0.05, 80% power, and equal group allocation, the minimum required sample size was eight evaluable mice per group.

For the *lnc-mg* cKO mice study, ten mice per group were included to allow for potential attrition during the six-month follow-up. All animals completed the study, with no mortality, exclusion, or sample loss. For the post-infarction study, ten mice were initially included in each treatment group to account for anticipated mortality during follow-up. Two mice in each group died after MI, leaving eight mice per group for the longitudinal echocardiographic analysis. These deaths were recorded as post-infarction mortality and were not treated as experimental exclusions.

Treadmill exercise testing

Exercise capacity was assessed using an incremental treadmill exhaustion test, with reference to previously described cardiovascular phenotyping procedures[26,27]. Mice were familiarized with the motorized treadmill before formal testing. During the exhaustion test, the treadmill was maintained at a 0° incline, with an initial speed of 9 m/min that was increased by 1 m/min every 2 min until exhaustion. Exhaustion was defined as the inability of a mouse to maintain the prescribed running speed despite repeated gentle encouragement. Running time was recorded from the initiation of the test until exhaustion, and total running distance was calculated as the cumulative distance completed during all successive speed stages. Longitudinal treadmill

testing was performed in the same cohort of mice at 2, 4, 6, and 8 months of age. Echocardiographic and treadmill assessments were conducted on separate days to minimize the potential influence of acute exercise on cardiac measurements.

MI model and adeno-associated virus injection

Two-month-old male C57BL/6 mice were anesthetized with 1.5% isoflurane. A left thoracotomy was performed through the fourth intercostal space, and the chest cavity was exposed using a retractor. Under microscopic guidance, the left anterior descending coronary artery was ligated approximately 2 mm below its origin using an 8-0 polypropylene suture. Successful myocardial ischemia was confirmed by the immediate pallor of the left ventricular anterior wall.

Adeno-associated virus 9 (AAV9) vectors carrying either *lnc-mg* or luciferase under the control of the *cTnT* promoter were constructed by WZ Biosciences. Immediately after coronary ligation, AAV9-*lnc-mg* or AAV9-Luc was administered by intramyocardial injection at a dose of 1×10^{10} vector genomes (vg) per mouse in a total volume of 10 μL. The thoracic cavity was then closed, followed by suturing of the muscle and skin layers.

Eligible animals were two-month-old male C57BL/6 mice with successful induction of myocardial ischemia, as confirmed by the immediate appearance of pallor in the left ventricular anterior wall after coronary ligation. Prespecified exclusion criteria included unsuccessful MI induction or technical failure that prevented reliable data acquisition. No animals were excluded on these grounds. Animals that died during post-infarction follow-up were recorded as post-infarction mortality rather than experimental exclusions.

Isolation of adult mouse cardiac tissue and myostation-intact myocardial contraction force measurement

Myocardial contractile force was measured using the Myostation-Intact system according to a previously described protocol[28]. Briefly, following euthanasia, the hearts were rapidly excised and placed in pre-cooled oxygenated Tyrode's solution containing 120 mM NaCl, 5.4 mM KCl, 1.2 mM NaH_2PO_4, 5.6 mM glucose, 10 mM HEPES, 3.4 mM $MgCl_2$, 5 mM taurine, 1.5 mM $CaCl_2$, and 30 mM BDM, adjusted to pH 7.35-7.45. The left ventricular anterior wall was isolated, and myocardial strips (approximately 1 mm × 3 mm) were cut. These strips were placed in a Myostation-intact tissue bath, continuously perfused with 95% oxygen and 5% carbon dioxide gas mixture. At 37 °C, myocardial contractility was assessed through graded voltage (5-10 V) stimulation and graded calcium ion concentrations (1.5-7.5 mM) to evaluate myocardial contraction force[28].

Six independent mice were examined per group, with each mouse representing one biological replicate. No formal a priori power calculation was performed for this *ex vivo* assay. The sample size was informed by published murine studies employing six or a comparable number of independent animals per group for *ex vivo* measurements of papillary muscle contractile force[29,30], together with the technical requirements of the Myostation-Intact protocol, particularly the preparation and serial measurement of fresh, viable myocardial tissue[28].

Masson's trichrome staining and quantification of chronic post-infarction scar

At 56 days after MI, hearts were collected from three mice per treatment group. The mice were randomly selected from those surviving to day 56 before histological processing, without reference to echocardiographic measurements or other experimental outcomes. The sample size was informed by comparable published studies in which Masson's trichrome staining and histological assessment of chronic post-infarction remodeling were performed using three independent mice per group[31,32].

The excised hearts were rinsed in phosphate-buffered saline (PBS; NCM Biotech, C500C1), fixed in 4% paraformaldehyde (Servicebio, G1101-500ML) at 4 °C for 48 h, dehydrated through graded ethanol, cleared in xylene, and embedded in paraffin. Hearts were serially sectioned transversely, perpendicular to the cardiac long axis, at a thickness of 5 μm. To assess the longitudinal distribution of the scar, anatomically matched sections were sampled at four levels spanning the coronary ligation site to the apex, with an interval of 300 μm between consecutive levels. For quantitative analysis, one structurally intact section at the mid-ventricular level, defined as the midpoint between the ligation site and the apex, was examined from each mouse.

Following deparaffinization and rehydration, sections were stained using a Trichrome Stain (Masson) Kit (Sigma-Aldrich, HT15-1KT) and Weigert's Iron Hematoxylin Set (Sigma-Aldrich, HT1079-1SET) according to the manufacturer's instructions. Briefly, nuclei were stained with Weigert's iron hematoxylin, whereas the cytoplasm and viable myocardium were stained with Biebrich scarlet-acid fuchsin. Collagen was differentiated using phosphomolybdic-phosphotungstic acid and counterstained with aniline blue. The sections were subsequently differentiated in 1% acetic acid, dehydrated through graded ethanol, cleared in xylene, and mounted with a resin-based mounting medium (Fisher Chemical, SP15-100). Whole-section bright-field images were acquired using ZEISS Axioscan 7, with identical acquisition settings applied across all experimental groups.

Scar quantification was performed using a length-based method as previously described[33]. Measurements were conducted using ImageJ v1.54 (National Institutes of Health, Bethesda, MD, USA). The epicardial scar length, endocardial scar length, total left ventricular epicardial circumference, and total left ventricular endocardial circumference were manually traced. The epicardial scar length was defined as the length of the transmural collagenous scar along the epicardial surface, whereas the endocardial scar length was defined as the length of the endocardial surface over which scar tissue occupied more than 50% of the ventricular wall thickness. The scar circumference ratio was determined by averaging the proportions of the left ventricular epicardial and endocardial circumferences occupied by scar tissue. A single value was obtained for each mouse, and the individual mouse was treated as the independent biological replicate. Section selection and scar quantification were performed by an investigator blinded to the treatment allocation.

Langendorff perfusion for isolation of adult mouse cardiomyocytes

Hearts from 2-month-old *lnc-mg* cKO and *lnc-mg*$^{fl/fl}$ mice were rapidly excised, cannulated via the aorta, and placed in a Langendorff perfusion system. For cardiomyocyte isolation, a separate calcium-free, HEPES-buffered Tyrode's solution was used. To remove residual blood, the hearts were perfused for 5 min at 37 °C with calcium-free Tyrode's solution at a flow rate of 5-6 mL/min. The solution contained 130 mM NaCl, 5.4 mM KCl, 1 mM $MgCl_2$, 0.6 mM Na_2HPO_4, 10 mM glucose, and 10 mM HEPES and was adjusted to pH 7.4. Subsequently, a digestion solution containing type II collagenase (Worthington Biochemical Corporation, LS004176, 1 mg/mL) was used for 8-12 min, allowing softening of the ventricular wall. The heart was then removed, the ventricle separated, and cells dispersed by gentle mechanical disruption. After filtration, cells were repolarized through a stepwise increase in calcium ion concentration. Cells were collected by low-speed centrifugation and assessed for morphology by microscopy.

Assessment of adult mouse cardiomyocyte contractility

Ventricular cardiomyocytes were isolated from 2-month-old *lnc-mg* cKO and *lnc-mg*$^{fl/fl}$ mice using the Langendorff perfusion system. Cells were resuspended in plating medium (M199; Sigma-Aldrich, M4530) supplemented with 10 mM 2,3-butanedione monoxime (BDM; Sigma-Aldrich, B0753) and 5% fetal bovine serum (Gibco, A5669801), and seeded onto laminin-coated dishes or confocal plates pre-coated with 20 μg/mL laminin (Gibco, 23017015) for 1 h at 37 °C in a CO_2 incubator. Only rod-shaped cardiomyocytes

with clear striations and no spontaneous contractions were selected for functional measurements. Sarcomere shortening and maximum shortening velocity (+dL/dt max) were recorded simultaneously using the Multi-Cell Lite® system (IonOptix LLC, Westwood, MA, USA), with field stimulation at 1 Hz and 10 V at 37 °C. Data from ten consecutive contraction cycles per cell were acquired and analyzed using CytoSolver 3.0 software (IonOptix LLC)[8,30,34]. Ten consecutive contraction cycles were averaged to generate a single value for each cardiomyocyte. A total of 60 cardiomyocytes obtained from three independent mice were analyzed per group (n = 3 biological replicates). For graphical presentation, the 60 cell-level values were displayed collectively to show the distribution of individual cardiomyocyte measurements. For statistical inference, cardiomyocytes obtained from the same mouse were treated as observations nested within their mouse of origin, and group comparisons were performed using nested t-tests with the mouse serving as the biological replicate and experimental unit[8,30,34]. Individual cardiomyocytes were not treated as independent biological replicates.

Isolation and culture of neonatal mouse cardiomyocytes (NMCMs)

NMCMs were isolated from P1 C57BL/6 mice using a Neonatal Cardiomyocyte Isolation Kit (Miltenyi Biotec, 130-100-825) according to the manufacturer's instructions. Briefly, hearts were excised, minced, and enzymatically dissociated to obtain a single-cell suspension. Isolated cardiomyocytes were cultured in DMEM (Gibco, 11500596) supplemented with 10% fetal bovine serum (Gibco, A5669801) at 37 °C in a humidified atmosphere containing 5% CO_2. Cells were allowed to recover for 24 h before subsequent adenoviral transduction or siRNA-mediated knockdown.

Adenovirus-mediated overexpression of *lnc-mg* in NMCMs

For *lnc-mg* overexpression, NMCMs were transduced with an adenoviral vector expressing *lnc-mg* (Ad-*lnc-mg*) or the corresponding control adenovirus (Ad-Ctrl). Adenoviral vectors were constructed by Hanheng Biotechnology. Cells were transduced at a multiplicity of infection of 1, and the culture medium was replaced 24 h after transduction. Overexpression efficiency was confirmed by RT-qPCR before functional assessment.

siRNA-mediated knockdown of Mbnl1 in NMCMs

For *Mbnl1* knockdown, NMCMs were transfected with 50 nM *Mbnl1*-targeting siRNA (si*Mbnl1*) or non-targeting control siRNA (si*NC*) using Lipofectamine RNAiMAX (Thermo Fisher Scientific, 13778075) according to the manufacturer's instructions. For combined gain- and loss-of-function experiments, cells were assigned to four groups: control adenovirus with si*NC*, Ad-*lnc-mg* with si*NC*, control adenovirus with si*Mbnl1*, or Ad-*lnc-mg* with si*Mbnl1*. Knockdown efficiency was verified by RT-qPCR before contractile function analysis.

CardioExcyte 96 assessment of cardiomyocyte contractile function

Three independent NMCM isolations were performed on separate occasions, each using a distinct pool of ventricular cardiomyocytes obtained from 20 P1 neonatal mice. Each pooled cell isolation constituted one independent biological replicate. For each experiment, NMCMs were assigned to the four treatment conditions described above and seeded at 1×10^5 cells per well in CardioExcyte 96 plates (Nanion Technologies), with 24 technical replicate wells per condition. Spontaneous contractile activity was monitored using the CardioExcyte 96 platform by label-free impedance recording. Measurements were acquired for 30 s at 2-h intervals over a total monitoring period of 120 h. Beat rate, contractile amplitude, and upstroke velocity were quantified using CardioExcyte Control 96 and DataControl 96 software.

Within each independent isolation, measurements from the 24 technical replicate wells were first averaged at each recording time point, and the resulting 60 time-point means were subsequently averaged over the complete monitoring period to generate one summary value per condition. Individual wells and serial

recording time points were treated as technical replicates and repeated measurements, respectively, rather than as independent observations. All three experiments were conducted using identical cell-seeding densities, treatment conditions, culture procedures, and recording settings.

RNA immunoprecipitation (RIP) assay

RIP assay was performed using the commercially available Magna RIP RNA-binding protein (RBP) Immunoprecipitation Kit (Sigma-Aldrich, 17-700) according to the manufacturer's standard protocol to identify the interaction between target RNA and RBP in mammalian cells.

Briefly, adult mouse cardiomyocytes were isolated via Langendorff perfusion, washed with pre-chilled nuclease-free PBS, and immediately lysed in ice-cold RIP lysis buffer containing protease and RNase inhibitors. Protein lysates were incubated on ice, centrifuged at 14,000 g for 10 min at 4 °C to remove debris, and the resulting 100 μL supernatants were collected, with a 10 μL aliquot reserved as the 10% input for RNA normalization. For each immunoprecipitation, protein A/G magnetic beads supplied with the kit were conjugated with 5 μg of anti-MBNL1 antibody (Cell Signaling Technology, 46160S), anti-CELF1 antibody (Abcam, ab129115), or normal rabbit IgG supplied with the kit (MilliporeSigma, PP64B). The antibody-bead complexes were subsequently incubated with cardiomyocyte lysates overnight at 4 °C with gentle rotation. The bead-bound complexes were then extensively washed with cold kit-provided RIP wash buffer to remove non-specific contaminants.

Purified co-precipitated RNAs were then extracted from immunoprecipitated complexes. RT-qPCR was performed to quantify target RNA enrichment in IP samples relative to IgG controls. All experiments were conducted in biological triplicates. Relative RNA binding enrichment was normalized to the input control to assess specific protein-RNA interactions.

Immunofluorescence staining, confocal imaging, and quantitative analysis of MBNL1 nuclear localization

Cardiomyocytes were fixed with 4% paraformaldehyde at room temperature for 10 min, permeabilized with 0.3% Triton X-100 in PBS, and blocked with 5% donkey serum for 1 h at room temperature. Cells were incubated overnight at 4 °C with primary antibodies against MBNL1 (Cell Signaling Technology, 46160S, 1:200) and α-actinin (Abcam, ab9465, 1:400). This was followed by incubation for 1 h at room temperature with highly cross-adsorbed Alexa Fluor 488-conjugated donkey anti-mouse IgG (H + L) (Thermo Fisher Scientific, Cat. No. A-21202; RRID: AB_141607) and highly cross-adsorbed Alexa Fluor 647-conjugated donkey anti-rabbit IgG (H + L) (Thermo Fisher Scientific, Cat. No. A-31573; RRID: AB_2536183), both diluted 1:800 in PBS. Nuclei were counterstained with 4′,6-diamidino-2-phenylindole (DAPI)-containing mounting medium (Thermo Fisher Scientific, P36966).

Images were acquired using a ZEISS LSM 880 confocal laser-scanning microscope under identical imaging settings for all experimental groups. Laser power, detector gain, pinhole size, image resolution, and all other acquisition settings were maintained identically across experimental groups. For each cardiomyocyte, a z-stack comprising five optical sections at 1-μm intervals was collected, from which a maximum-intensity projection was generated for quantitative analysis.

Nuclear regions of interest were defined based on DAPI staining, whereas whole-cell boundaries were delineated according to α-actinin staining. Following background subtraction, the mean MBNL1 fluorescence intensity was measured separately in the nuclear and cytoplasmic compartments using ImageJ 1.54 within the Fiji distribution (National Institutes of Health, Bethesda, MD, USA). MBNL1 nuclear localization was expressed as the ratio of nuclear to cytoplasmic mean fluorescence intensity.

Fifty cardiomyocytes were analyzed from each mouse. Measurements from the cardiomyocytes derived from the same mouse were averaged to generate a single mouse-level value. Accordingly, each mouse constituted one independent biological replicate, whereas individual cardiomyocytes derived from the same mouse were treated as nested observations and were not considered independent biological replicates.

RNA extraction and RT-qPCR

Total RNA was extracted from cultured cells or cardiac tissues using TRIzol reagent (Thermo Fisher Scientific) according to the manufacturer's instructions. RNA concentration and purity were assessed using a NanoDrop spectrophotometer (Thermo Fisher Scientific). For each sample, 1 μg of total RNA was reverse-transcribed into cDNA using a reverse transcription kit (Vazyme, catalog no. R323-01) on a T100 Thermal Cycler (Bio-Rad).

Quantitative PCR was performed using the hydrolysis probe method on a QuantStudio 5 Real-Time PCR System (Applied Biosystems, Thermo Fisher Scientific). Each reaction was prepared in a total volume of 12 μL, containing 6 μL of 2× TaqMan Fast Advanced Master Mix (Thermo Fisher Scientific), 1 μL of the gene-specific primer-probe mixture, and 5 μL of cDNA containing 5 ng of template. Amplification was performed for 35 cycles at 95 °C for 30 s, 60 °C for 10 s, and 72 °C for 30 s. Each biological sample was analyzed in technical triplicate. No-template and no-reverse-transcription controls were included to monitor potential contamination and nonspecific amplification.

The hydrolysis probes were custom-designed and synthesized by GenePharma. The *lnc-mg* probe was labeled with 6-FAM at the 5′ end and TAMRA-N at the 3′ end, with the sequence 5′-AAGATTTCCTAGGGTACAGGCAAAGGC-3′. The complete primer and probe sequences are provided in Supplementary Data 1. Gene expression was normalized to 18S rRNA and calculated using the $2^{-\Delta\Delta Ct}$ method, with the corresponding control group in each experiment serving as the calibrator.

Bulk RNA sequencing and transcriptomic analysis

Total RNA was extracted from myocardial tissue in 2-month-old *lnc-mg* cKO mice and *lnc-mg*$^{fl/fl}$ mice and subjected to bulk RNA sequencing. Three independent mice were included per genotype, with each sequencing library prepared from an individual mouse without sample pooling. The number of biological replicates was determined with reference to comparable published bulk RNA-sequencing studies and the availability of biological samples meeting the prespecified quality requirements. Selected transcriptomic alterations related to cardiomyocyte contractile function were subsequently validated by RT-qPCR.

Gene-level expression was quantified using RNA-seq by expectation-maximization, and the resulting expected counts were rounded to the nearest integers. Genes with counts ≥ 10 in at least three samples were retained for subsequent analysis.

All analyses were performed in R version 4.4.1. Differential gene expression analysis was performed using the DESeq2 package (v1.46.0). Gene-level expected count matrices were imported using the DESeqDataSetFromMatrix function, followed by normalization, dispersion estimation, and differential expression analysis using the standard DESeq2 workflow[35]. Log2 fold-change estimates were shrunk using the lfcShrink function with the normal prior estimator (type = "normal")[35]. Genes with a Benjamini-Hochberg-adjusted *P* value (padj) < 0.05 were considered differentially expressed. Variance-stabilizing transformation (VST) was performed using the vst function for downstream visualization and clustering analyses.

Principal component analysis (PCA) was performed using the prcomp function in R based on VST-transformed expression matrices. Sample clustering was visualized using ggplot2 (v4.0.2) and ggrepel (v0.9.8). Unsupervised hierarchical clustering of differentially expressed genes was performed using row-scaled VST-transformed expression values and visualized with the pheatmap (v1.0.13).

Functional enrichment analysis was performed using clusterProfiler (v4.14.6), AnnotationDbi (v1.68.0), and the org.Mm.eg.db annotation database (v3.20.0). Gene ontology (GO) Biological Process enrichment analysis was conducted separately for upregulated and downregulated differentially expressed genes using the enrichGO function. GO enrichment analysis of MBNL1-bound transcripts derived from public heart CLIP-seq datasets was performed using the same analytical workflow. *P* values were adjusted using the Benjamini-Hochberg method, and enriched GO terms were visualized using ggplot2.

Gene set enrichment analysis (GSEA) was performed using the fgsea (v1.35.6). Transcriptome-wide ranked gene lists were generated from DESeq2 differential expression statistics, and gene sets were obtained from the Molecular Signatures Database (MSigDB, v26.1.0) through the msigdbr package. Hallmark and GO collections were used for enrichment analysis, including Hallmark Myogenesis and GO Muscle System Process. Enrichment significance was evaluated using normalized enrichment scores (NES) and adjusted *P* values.

Integrative bioinformatic prediction of lnc-mg-associated RBPs

Candidate RBPs potentially associated with *lnc-mg* were identified using an integrative bioinformatic workflow. Putative *lnc-mg*-protein interactions were first retrieved from the ENCORI database (https://rna.sysu.edu.cn/encori/) and RNAInter database (http://www.rnainter.org/)[36,37]. Candidate RBPs identified from either database were then further evaluated using the RPISeq web server (http://pridb.gdcb.iastate.edu/RPISeq/), which predicts RNA-protein interaction probabilities based on primary sequence features using random forest (RF) and support vector machine (SVM) classifiers[38]. Proteins with an RF score > 0.90 and an SVM score > 0.60 were considered high-confidence candidate *lnc-mg*-associated RBPs and were selected for subsequent experimental validation.

Molecular docking analysis

The full-length *lnc-mg* transcript was segmented into six overlapping fragments for independent structural prediction and molecular docking analysis. RNA secondary structures of each fragment were predicted using RNAfold based on the minimum free energy model implemented in the ViennaRNA package. The resulting dot-bracket secondary structures were submitted to RNAComposer to generate three-dimensional RNA models in PDB format. The complete *lnc-mg* sequence, fragment coordinates, RNA secondary structures, ViennaRNA prediction files, and three-dimensional structural models are provided in Supplementary Data 2.

The three-dimensional structure of mouse MBNL1 was obtained from the AlphaFold Protein Structure Database based on the UniProt entry Q9JKP5 (MBNL1, Mus musculus). Molecular docking between each *lnc-mg* fragment and MBNL1 was performed independently using the HDOCK server with default parameters. Docking models were ranked according to docking score, and the highest-ranked docking complex was selected for subsequent interface analysis. Predicted interacting RNA nucleotides, MBNL1 amino acid residues, and hydrogen-bond contacts were analyzed from the selected docking model. Canonical MBNL1 recognition motifs (YGCY) were mapped onto the *lnc-mg* sequence and compared with the predicted docking interface. Structural visualization and interface residue mapping were performed using PyMOL.

Statistical analysis

Unless otherwise specified, n represents the number of independent biological replicates. For *in vivo* experiments, each mouse was considered an independent biological replicate. For experiments using adult cardiomyocytes, the mouse from which the cells were isolated served as the biological replicate, whereas individual cardiomyocytes obtained from the same mouse were treated as nested observations. For the IonOptix analyses, group differences in maximum shortening velocity (+dL/dt max) and sarcomere shortening were evaluated using nested t-tests, with individual cardiomyocytes nested within their mouse of origin and the mouse treated as the experimental unit[8,30,34]. For neonatal cardiomyocyte experiments, each independently prepared cell isolation generated from a distinct pool of P1 neonatal mice was considered one biological replicate, whereas replicate wells derived from the same isolation were treated as technical replicates. For CardioExcyte 96 analysis, technical-well measurements and serial recordings were averaged within each isolation to generate one isolation-level summary value per condition. Isolation-level values from the four treatment conditions were analyzed using two-way repeated-measures ANOVA, with adenoviral and siRNA treatments treated as within-isolation factors and each independent isolation as the matched experimental unit, followed by Šídák's multiple-comparisons test. In myocardial strip experiments, the mouse of origin was considered the biological replicate, with multiple strips obtained from the same mouse treated as nested measurements. Repeated contraction cycles from the same cell or myocardial strip, serial measurements from the same animal, and repeated recordings from the same well were not considered independent replicates. Technical replicates obtained under the same experimental condition were averaged within each biological replicate before statistical analysis, whereas longitudinal measurements were retained and analyzed as repeated observations. The exact definition of n, together with the numbers of biological replicates and any technical or nested measurements, is provided in the corresponding method subsection and figure legends.

All data are presented as the mean ± standard error of the mean (SEM). Comparisons between two groups were made using Student's *t*-test. Multiple unpaired t-tests were used to compare the expression of individual genes between *lnc-mg* cKO and control mice in the RT-qPCR validation experiment. One-way ANOVA followed by Bonferroni's multiple-comparisons test was used for single-factor comparisons involving more than two groups. Ordinary two-way ANOVA followed by Tukey's multiple-comparisons test was used for two-factor analyses involving independent observations.

Serial measurements obtained from the same animals were analyzed using repeated-measures two-way ANOVA, with genotype or treatment as the between-subject factor and time as the within-subject factor. The Geisser-Greenhouse correction was applied without assuming sphericity, followed by Šídák's multiple-comparisons test for between-group comparisons at individual time points.

Statistical significance was defined as $P < 0.05$. All statistical analyses were performed using GraphPad Prism software (version 10.0).

RESULTS

lnc-mg is enriched in cardiomyocytes and sustains cardiac function

To characterize the expression profile of *lnc-mg*, we assessed its expression across diverse tissues from adult WT mice. *Lnc-mg* was predominantly expressed in skeletal muscle and heart, consistent with previous reports[20] [Figure 1A]. Notably, in the heart, *lnc-mg* expression increased progressively during postnatal development [Figure 1B], suggesting a potential role in postnatal cardiac maturation. To further define the cell type-specific expression of *lnc-mg*, we isolated cardiomyocytes and non-cardiomyocytes from 2-month-old WT mice via Langendorff perfusion. Cell-type expression analysis revealed that *lnc-mg* was enriched in cardiomyocytes but was nearly undetectable in non-cardiomyocytes [Figure 1C], indicating that *lnc-mg* primarily participates in the regulation of cardiomyocyte function in the heart.

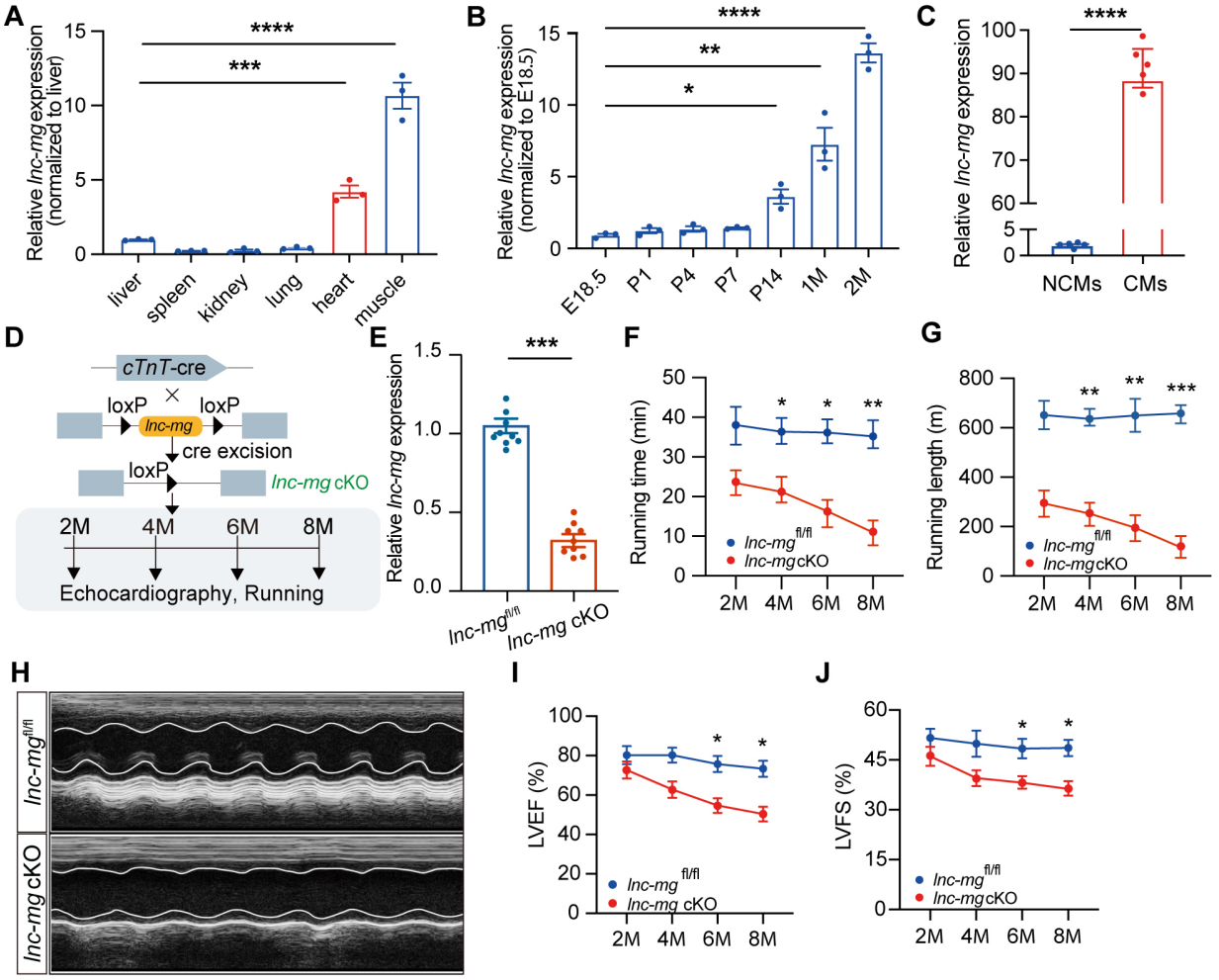

Figure 1. Cardiac expression profile of *lnc-mg* and phenotypic characterization of cardiomyocyte conditional knockout *lnc-mg* mice. (A) Relative expression of *lnc-mg* in different tissues from adult wild-type (WT) mice determined by RT-qPCR. Tissues from three independent mice were analyzed (n = 3 biological replicates). (B) Developmental expression of *lnc-mg* in mouse hearts at the indicated developmental stages, including embryonic day 18.5 (E18.5), postnatal day 1 (P1), P4, P7, P14, 1 month of age (1M), and 2M. Three independent hearts were analyzed at each developmental stage (n = 3 biological replicates per stage). (C) Relative expression of *lnc-mg* in isolated cardiomyocytes (CMs) and non-cardiomyocytes (NCMs) from adult mouse hearts. Paired CM and NCM fractions obtained from five independent mice were analyzed (n = 5 biological replicates). (D) Schematic illustrating the generation of *lnc-mg* cKO mice by crossing *lnc-mg*$^{fl/fl}$ mice with *cTnT*-Cre mice and the experimental design for subsequent phenotypic analyses. (E) RT-qPCR validation of *lnc-mg* deletion in *lnc-mg* cKO hearts in 2-month-old mice, n = 10 per group. (F and G) Longitudinal assessment of treadmill exercise performance of *lnc-mg*$^{fl/fl}$ and *lnc-mg* cKO mice at 2, 4, 6, and 8 months of age. Running time (F) and running distance (G) are shown. Ten independent mice were analyzed (n = 10 biological replicates). (H) Representative M-mode echocardiographic images of *lnc-mg*$^{fl/fl}$ and *lnc-mg* cKO mice at 8 months of age. (I and J) Serial echocardiographic assessment of left ventricular ejection fraction (LVEF) (I) and left ventricular fractional shortening (LVFS) (J) in *lnc-mg*$^{fl/fl}$ and *lnc-mg* cKO mice from 2 to 8 months of age. Ten independent mice were analyzed (n = 10 biological replicates). Measurements obtained from the same mouse at different ages were treated as repeated measurements. Data are presented as mean ± SEM. *P < 0.05; **P < 0.01; ***P < 0.001; ****P < 0.0001.

To evaluate the effect of *lnc-mg* in the heart, we generated cardiomyocyte-specific *lnc-mg* knockout mice (*lnc-mg* cKO) by crossing *lnc-mg*$^{fl/fl}$ mice with *cTnT*-Cre mice [Figure 1D]. RT-qPCR analysis confirmed a marked downregulation of *lnc-mg* expression in the heart of cKO mice at 2 months of age [Figure 1E]. Treadmill exercise testing showed that *lnc-mg* cKO mice exhibited significantly reduced running times and running distances compared with *lnc-mg*$^{fl/fl}$ mice [Figure 1F and G], suggesting impaired motor performance.

To determine whether cardiomyocyte-specific loss of *lnc-mg* induces cardiac dysfunction *in vivo*, we performed serial echocardiographic assessments from 2 to 8 months of age in *lnc-mg* cKO mice and *lnc-mg*$^{fl/fl}$ mice. Echocardiographic analyses revealed impaired systolic function in *lnc-mg* cKO mice, manifested by reduced LVEF and LVFS compared with *lnc-mg*$^{fl/fl}$ mice [Figure 1H-J]. Collectively, these findings identify *lnc-mg* as a cardiomyocyte-enriched lncRNA in the heart that contributes to the maintenance of cardiac function.

lnc-mg deficiency suppresses contractile machinery gene programs

To investigate the molecular basis of cardiac dysfunction in *lnc-mg* cKO mice, RNA sequencing of myocardial tissue from 2-month-old *lnc-mg* cKO and *lnc-mg*$^{fl/fl}$ mice was performed to characterize the transcriptomic differences associated with *lnc-mg* deficiency [Figure 2A]. PCA identified genotype-dependent clustering of cardiac transcriptomes, with control and *lnc-mg* cKO samples forming clearly separated groups [Figure 2B].

Differential expression analysis identified 185 genes exhibiting significant expression changes in *lnc-mg* cKO mouse hearts, including 66 upregulated and 119 downregulated genes [Figure 2C, Supplementary Data 3]. Unsupervised hierarchical clustering based on these differentially expressed genes readily distinguished cKO samples from controls, further highlighting the coordinated transcriptional remodeling associated with *lnc-mg* deficiency [Figure 2C, Supplementary Data 3]. Notably, a substantial proportion of downregulated genes were functionally related to sarcomeric organization and muscle contraction. Consistent with this observation, GO enrichment analysis demonstrated that genes downregulated in *lnc-mg* cKO heart were significantly concentrated in biological processes related to myofibril assembly, muscle system process, muscle contraction, actomyosin organization, and striated muscle cell development [Figure 2D, Supplementary Data 3]. Collectively, these categories converged on the structural and functional components of the cardiac contractile machinery.

Extending these observations beyond individual differentially expressed genes, GSEA revealed significant negative enrichment of the Myogenesis and Muscle System Process gene sets in *lnc-mg* cKO mouse hearts [Figure 2E and F, Supplementary Data 3]. To further validate the RNA-seq findings, we performed RT-qPCR analysis of ten representative genes associated with cardiac contractility, myogenesis, and myofibril assembly. Among the genes examined, *Myh7*, *Mybpc3*, and *Acta1* were significantly downregulated in *lnc-mg* cKO mouse hearts, providing independent validation of representative contractility-related alterations identified by RNA-seq [Supplementary Figure 1]. The RNA-seq differential expression statistics for the selected genes are provided in Supplementary Data 3. Together, these transcriptomic and RT-qPCR findings support the suppression of cardiac contractile and myofibrillar gene programs following *lnc-mg* deletion.

Cardiomyocyte-specific deletion of *lnc-mg* impairs myocardial contractility

To further determine whether the cardiac dysfunction observed in *lnc-mg* cKO mice was attributable to contractile deficits, we conducted a comprehensive assessment of myocardial contractility using both *ex vivo* tissue preparations and isolated single cardiomyocytes, as schematically illustrated in Figure 3A. At the cardiac tissue level, myocardial tissue was isolated from *lnc-mg* cKO and *lnc-mg*$^{fl/fl}$ mice, and the Myostation-intact system was used to assess tissue contraction function[28]. The results showed that, under graded voltage (5-10 V) stimulation, myocardial contractility in *lnc-mg* cKO mice was significantly lower than that in the control group, with a markedly reduced response to electrical stimulation [Figure 3B]. This contractile deficit persisted under increasing extracellular calcium concentrations (1.5-7.5 mM). Although myocardial force increased in both groups with increasing Ca^{2+} concentration, force generation remained consistently lower in *lnc-mg* cKO tissues across the entire concentration range [Figure 3C], indicating a diminished contractile response to extracellular Ca^{2+} stimulation.

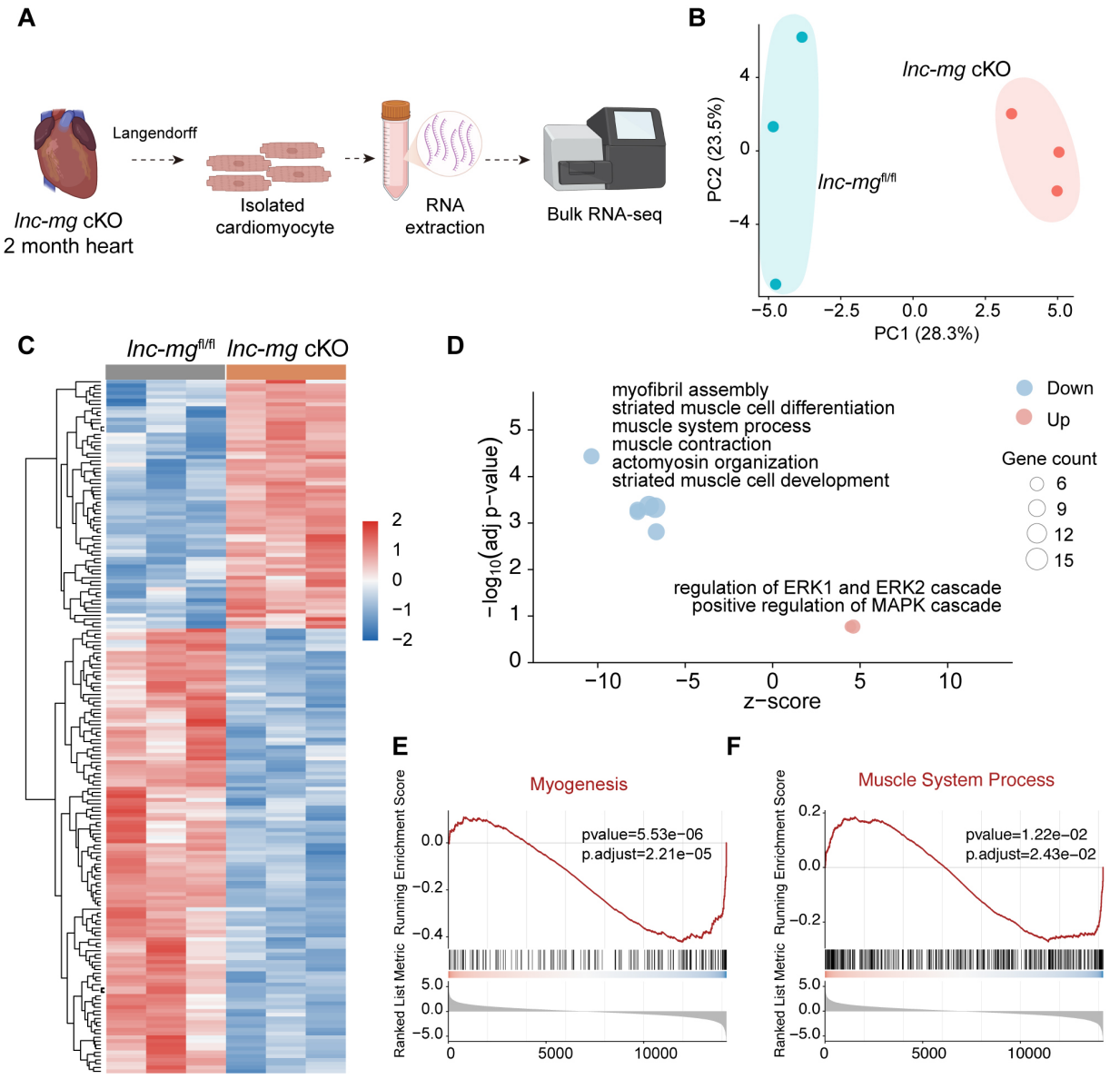

Figure 2. Transcriptomic analyses reveal suppression of contractile gene programs in *lnc-mg*-deficient hearts. (A) Schematic illustration of the experimental workflow. Myocardial tissues were collected from 2-month-old *lnc-mg*$^{fl/fl}$ and *lnc-mg* cKO mice, followed by RNA-seq. Created in BioRender. Jia S, (2026) htt ps://BioRender.com/umio76p. (B) PCA of RNA-seq samples from *lnc-mg*$^{fl/fl}$ and *lnc-mg* cKO hearts. Three independent mice were analyzed per genotype (n = 3 biological replicates per group). (C) Heatmap showing the expression patterns of differentially expressed genes identified between *lnc-mg*$^{fl/fl}$ and *lnc-mg* cKO hearts. Gene expression values were row-scaled for visualization. (D) GO enrichment analysis of upregulated and downregulated genes. Bubble size represents gene count, and bubble color indicates upregulated or downregulated gene sets. (E and F) GSEA of the Myogenesis gene set (E) and the Muscle System Process gene set (F) using genes ranked according to DESeq2 statistics. All transcriptomic analyses were based on the same three independent biological replicates per group.

To assess contractile function at the single-cell level, ventricular cardiomyocytes were isolated from 2-month-old *lnc-mg*$^{fl/fl}$ and *lnc-mg* cKO mice [Figure 3D], and sarcomere dynamics were measured using the IonOptix platform[8,30,34]. Compared with cardiomyocytes isolated from *lnc-mg*$^{fl/fl}$ mice, *lnc-mg* cKO cardiomyocytes displayed significantly reduced maximum contraction rate (+dL/dt max) and sarcomere shortening [Figure 3E and F].

Collectively, these findings demonstrate that cardiomyocyte-specific loss of *lnc-mg* impairs contractile performance at both the myocardial tissue and single-cardiomyocyte levels, supporting an important role for *lnc-mg* in maintaining cardiac contractility.

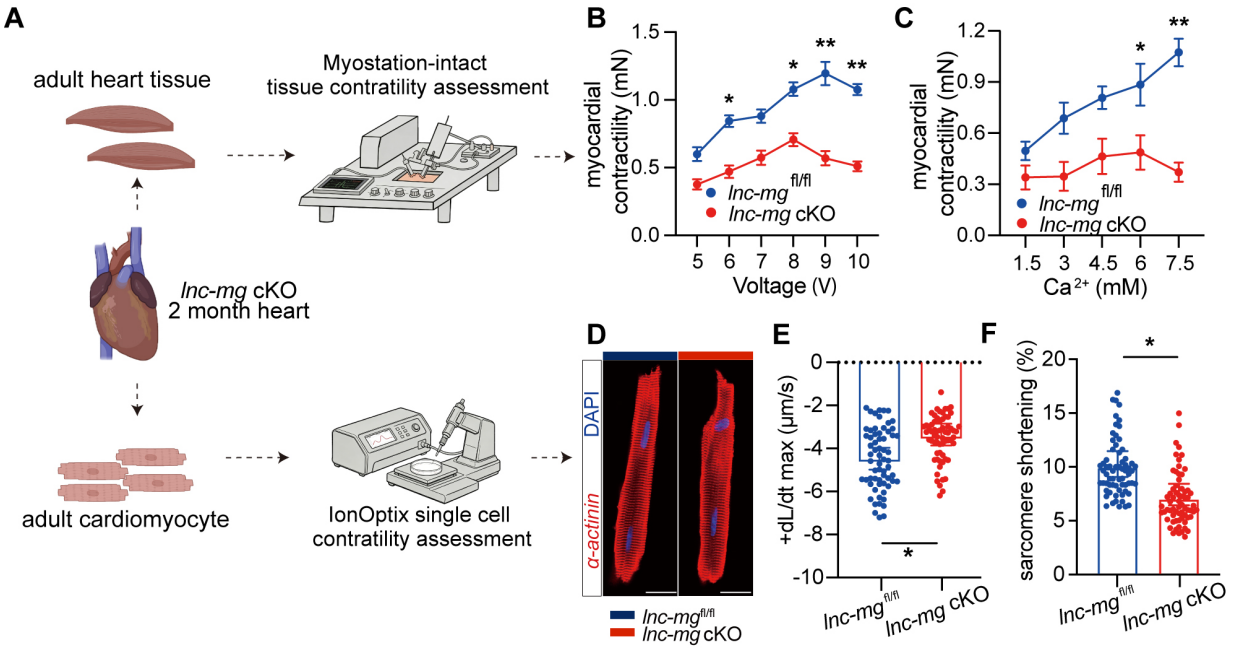

Figure 3. *Lnc-mg* deficiency impairs contractile function in myocardial tissue and isolated cardiomyocytes. (A) Schematic of myocardial tissue and single-cardiomyocyte contractility assessment using the Myostation-intact and IonOptix systems. Created in BioRender. Jia S, (2026) https://BioRender.com/0o3q3pu. (B and C) Contractile force of left ventricular myocardial strips isolated from 2-month-old *lnc-mg*$^{fl/fl}$ and *lnc-mg* cKO mice under graded electrical stimulation (5-10 V) (B) and increasing extracellular Ca^{2+} concentrations (1.5-7.5 mM) (C). Myocardial strips were obtained from six independent mice per group (n = 6 biological replicates per group), with the mouse serving as the experimental unit. Measurements obtained from the same myocardial preparation at different stimulation voltages or Ca^{2+} concentrations were treated as repeated measurements. (D) Representative immunofluorescence images of freshly isolated adult cardiomyocytes stained for α-actinin (red) and DAPI (blue), demonstrating the morphology of isolated rod-shaped cardiomyocytes before IonOptix analysis, Scale bar, 10 μm. (E and F) IonOptix analysis of maximum shortening velocity (+dL/dt max) (E) and sarcomere shortening (F) in isolated adult cardiomyocytes. The 60 points shown per group represent pooled cell-level measurements obtained from three independent mice (n = 3 biological replicates per group). Statistical comparisons were performed using nested t-tests, with cardiomyocytes nested within their mouse of origin. Data are presented as mean ± SEM. *P < 0.05; **P < 0.01.

Identification of MBNL1 as a lnc-mg-associated RBP linked to cardiomyocyte contractile programs

Given that interactions with RBPs represent a major mechanism by which lncRNAs regulate gene expression, we sought to identify RBPs that could potentially mediate the downstream molecular functions of *lnc-mg*. By integrating multiple complementary prediction platforms, including ENCORI, RNAInter, and RPISeq, MBNL1 and CELF1 were identified as the highest-confidence candidate interacting proteins [Figure 4A, Supplementary Data 4][36-38]. RIP assays further demonstrated that endogenous *lnc-mg* was specifically enriched in the MBNL1 immunoprecipitate, whereas no significant enrichment was detected with CELF1, supporting a selective association between *lnc-mg* and MBNL1 in mouse cardiomyocytes [Figure 4B and C].

To further characterize this association, structural prediction and molecular docking analyses were performed. Docking predicted a structurally plausible model of a putative *lnc-mg*-MBNL1 complex with a favorable binding energy and high confidence score, and the predicted interaction interface contained multiple hydrogen-bond contacts [Figure 4D]. Notably, the predicted docking interface overlapped with a cluster of accessible YGCY motifs, the canonical RNA recognition motif of MBNL1[39], supporting structural compatibility between *lnc-mg* and the RNA-binding interface of MBNL1 [Figure 4E].

As many established post-transcriptional regulatory functions of MBNL1 are closely associated with its nuclear localization, we next examined whether *lnc-mg* deficiency influences the subcellular distribution of MBNL1. Immunofluorescence analysis demonstrated that cardiomyocyte-specific deletion of *lnc-mg*

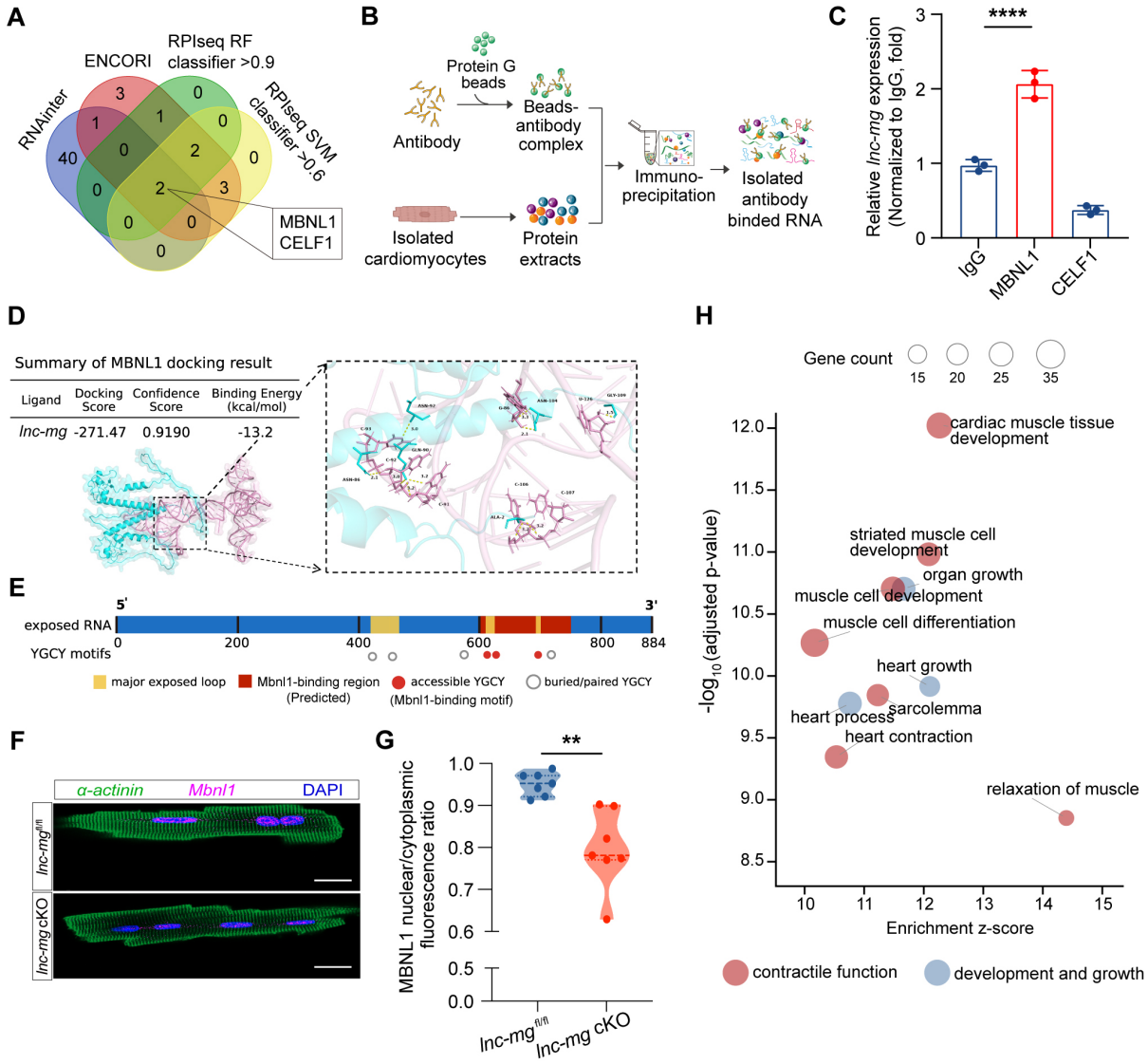

Figure 4. *Lnc-mg* is associated with MBNL1 and promotes its nuclear localization in cardiomyocytes. (A) Integrative prediction of *lnc-mg*-associated RNA-binding proteins using ENCORI, RNAInter, and RPISeq prediction platforms. (B) Schematic of the RNA immunoprecipitation (RIP) assay. Created in BioRender. Jia S, (2026) https://BioRender.com/cmx8vep. (C) RIP-qPCR analysis of *lnc-mg* enrichment following immunoprecipitation with IgG, MBNL1, or CELF1 antibodies from adult cardiomyocytes. Cardiomyocytes were obtained from three independent mice (n = 3 biological replicates). For each biological replicate, the same lysate preparation was divided among the IgG, MBNL1, and CELF1 immunoprecipitation conditions. (D) Predicted molecular docking model of a putative *lnc-mg*-MBNL1 complex, showing the docking score, confidence score, predicted binding energy, and an enlarged view of the predicted interaction interface with hydrogen-bond interactions. (E) Schematic of the predicted MBNL1-binding region and the distribution of canonical MBNL1 recognition motifs (YGCY) along the full-length *lnc-mg* transcript. (F) Representative immunofluorescence images showing MBNL1 subcellular localization in isolated adult cardiomyocytes from *lnc-mg*$^{fl/fl}$ and *lnc-mg* cKO mice. α-actinin (green), MBNL1 (magenta), and nuclei (DAPI, blue). Scale bar, 20 μm. (G) Quantification of the MBNL1 nuclear-to-cytoplasmic fluorescence intensity ratio in isolated adult cardiomyocytes. Fifty cardiomyocytes were analyzed from each of seven independent mice per group (n = 7 biological replicates per group). Measurements from the cardiomyocytes obtained from the same mouse were averaged to generate one mouse-level value. (H) GO enrichment analysis of MBNL1-bound transcripts identified from published heart MBNL1 CLIP-seq data. Bubble size represents gene count, and colors indicate functional categories. Data are presented as mean ± SEM. $^{**}P < 0.01$; $^{****}P < 0.0001$.

markedly reduced nuclear accumulation of MBNL1, accompanied by redistribution of MBNL1 toward the cytoplasm [Figure 4F and G].

To further characterize the functional features of MBNL1 in the heart, we analyzed publicly available heart CLIP-seq datasets[39]. GO enrichment analysis of MBNL1-bound transcripts demonstrated significant enrichment for biological processes associated with muscle contraction, sarcomere organization, myofibril

organization, sarcolemma organization, and muscle relaxation, indicating that MBNL1 preferentially associates with transcripts involved in cardiomyocyte contractile function [Figure 4H, Supplementary Data 5]. These biological processes were highly consistent with the contractile gene programs suppressed in *lnc-mg*-deficient hearts identified by RNA-seq [Figure 2], suggesting convergence between MBNL1-associated RNA regulation and the transcriptional and functional phenotype associated with *lnc-mg* deletion.

We next examined whether MBNL1 contributed to the effect of *lnc-mg* on cardiomyocyte contractility. NMCMs were transduced with an adenovirus expressing *lnc-mg* (Ad-*lnc-mg*) or a control adenovirus (Ad-Ctrl) in the presence of either *Mbnl1*-targeting or control siRNA. Contractile activity was monitored using the CardioExcyte 96 platform, which enables real-time impedance-based measurement of spontaneous beat rate, contractile amplitude, and upstroke velocity[40,41]. RT-qPCR verified efficient *lnc-mg* overexpression and *Mbnl1* knockdown [Supplementary Figure 2A-C].

In cardiomyocytes treated with control siRNA, *lnc-mg* overexpression increased contractile amplitude and upstroke velocity without affecting spontaneous beat rate. Following *Mbnl1* knockdown, these *lnc-mg*-associated increases in contractile amplitude and upstroke velocity were no longer observed, whereas beat rate remained unchanged across the experimental conditions [Supplementary Figure 2D-F]. These findings are consistent with a contribution of MBNL1 to the changes in cardiomyocyte contractile amplitude and contraction kinetics associated with *lnc-mg*.

Taken together, these complementary biochemical, structural, cellular, transcriptomic analyses, and loss-of-function findings suggest a model in which *lnc-mg* associates with MBNL1 for its regulation of cardiomyocyte contractile function.

lnc-mg attenuates post-infarction cardiac dysfunction and remodeling

Given the essential role of *lnc-mg* in maintaining myocardial contractility, we hypothesized that it might play a protective role after cardiac injury. To test this hypothesis, we generated a recombinant AAV9 vector expressing *lnc-mg* under the control of the *cTnT* promoter (hereafter referred to as AAV9-*lnc-mg*), together with a luciferase-expressing control vector (AAV9-*Luc*). WT mice aged 2 months received an intramyocardial injection of either AAV9-*lnc-mg* or AAV9-*Luc* on the same day as MI surgery, followed by serial echocardiographic monitoring [Figure 5A]. RT-qPCR analysis revealed that *lnc-mg* expression was significantly upregulated at 7 days post-MI (7 dpi) following AAV9-*lnc-mg* administration [Figure 5B].

Serial echocardiographic assessments showed that AAV9-*lnc-mg* treatment significantly preserved cardiac contractile function, as evidenced by higher LVEF and LVFS than those in the AAV9-*Luc* group [Figure 5C-E]. Histological examination of Masson's trichrome-stained heart sections further revealed a marked attenuation of post-infarction fibrosis in AAV9-*lnc-mg*-treated hearts, accompanied by substantial preservation of left ventricular architecture and myocardial wall integrity [Figure 5F]. Quantification at the mid-ventricular level showed that *lnc-mg* overexpression significantly reduced the scar circumference ratio [Figure 5G], suggesting that *lnc-mg* alleviates adverse ventricular remodeling after MI.

Moreover, *ex vivo* functional assessments of isolated myocardial strips demonstrated that *lnc-mg* overexpression significantly enhanced myocardial responsiveness to both electrical pacing and calcium stimulation, as reflected by increased contractile amplitude and improved force-generating capacity compared with AAV9-*Luc*-treated hearts [Figure 5H and I]. These findings indicate that *lnc-mg* not only attenuates structural remodeling after ischemic injury, but also improves myocardial contractile performance.

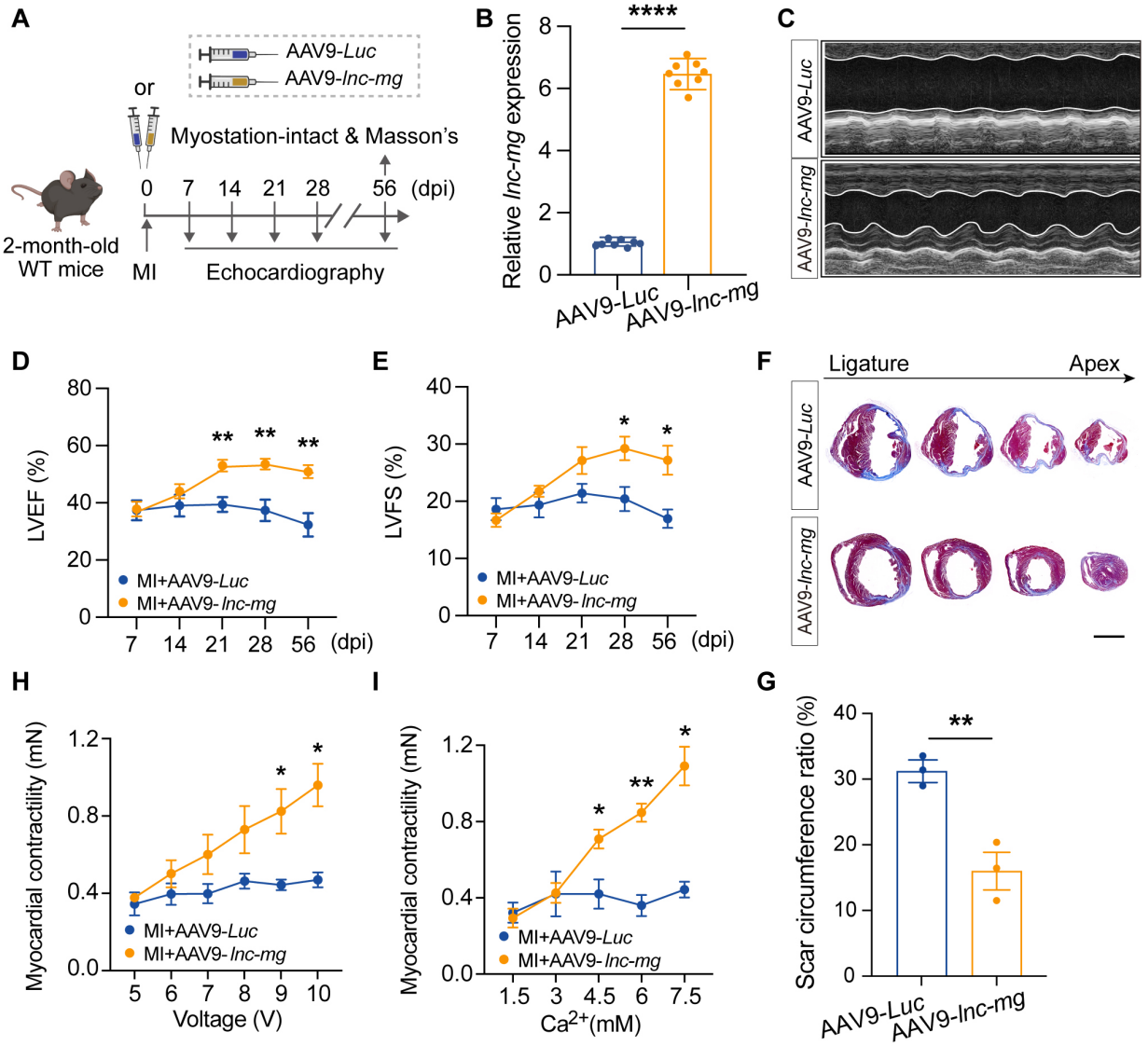

Figure 5. Cardiomyocyte overexpression of *lnc-mg* improves cardiac contractile function and attenuates myocardial remodeling after myocardial infarction. (A) Schematic of the mouse MI model, AAV9-mediated *lnc-mg* overexpression, and experimental timeline. Created in BioRender. Jia S, (2026) https://BioRender.com/6ylhd7s. (B) RT-qPCR validation of *lnc-mg* overexpression at 7 days post-MI (7 dpi). Eight independent mice were analyzed per treatment group (n = 8 biological replicates per group). (C-E) Representative M-mode echocardiographic images (C) and serial measurements of LVEF (D) and LVFS (E) from 7 to 56 days post-MI. The same cohort of mice was followed throughout the study (n = 8 mice per treatment group). Each mouse represented an independent biological replicate, and measurements obtained from the same mouse at different time points were treated as repeated measurements. (F and G) Representative serial transverse Masson's trichrome-stained heart sections collected at 56 days post-MI from the ligation site to the apex, with quantification of the scar circumference ratio at the mid-ventricular level (G). Sections from three independent mice were analyzed per treatment group (n = 3 biological replicates per group). Scale bar, 500 μm. (H and I) Myostation analysis of contractile force in left ventricular myocardial strips under graded electrical stimulation (5-10 V) (H) and increasing extracellular Ca^{2+} concentrations (1.5-7.5 mM) (I) at 56 days post-MI. Myocardial strips were obtained from six independent mice per treatment group (n = 6 biological replicates per group), with the mouse serving as the experimental unit. Measurements obtained from the same myocardial preparation at different stimulation voltages or Ca^{2+} concentrations were treated as repeated measurements. Data are presented as mean ± SEM. *P < 0.05; **P < 0.01; ****P < 0.0001.

Collectively, these results demonstrate that *lnc-mg* upregulation mitigates post-infarction cardiac dysfunction and structural remodeling, underscoring its potent cardioprotective role.

DISCUSSION

MI remains a major cause of persistent cardiac dysfunction and adverse ventricular remodeling[1-6]. Although substantial progress has been made in reperfusion and secondary prevention, restoration of the intrinsic contractile capacity of injured myocardium remains challenging. In this study, we identified the muscle-enriched lncRNA *lnc-mg* as a regulator of cardiomyocyte contractile function. Using a cardiomyocyte *lnc-mg* cKO mouse model, we found that *lnc-mg* depletion markedly impaired left ventricular systolic function. Transcriptomic profiling further showed that *lnc-mg* deficiency was accompanied by coordinated suppression of genes involved in myocardial contractility. Consistent with these findings, contractile function was impaired at both the myocardial tissue and single-cardiomyocyte levels in *lnc-mg* cKO mice. Mechanistically, we identified an association between *lnc-mg* and the RBP MBNL1 and found that *lnc-mg* deficiency markedly reduced MBNL1 nuclear accumulation, while MBNL1-bound transcripts were preferentially enriched in biological processes related to cardiomyocyte contractile function. Importantly, *lnc-mg* overexpression in cardiomyocytes attenuated post-infarction cardiac dysfunction and remodeling in mice. Together, these findings suggest that *lnc-mg* contributes to the maintenance of the contractile program in mouse heart.

Cardiac lncRNAs have been implicated in diverse aspects of myocardial homeostasis and disease[42]. In the setting of MI, many reported lncRNAs influence cardiac repair and remodeling by regulating cardiomyocyte proliferation, mitochondrial integrity, fibrosis, or neovascularization[43-48]. In comparison, the direct regulation of cardiomyocyte contractility by lncRNAs has received considerably less attention.

Research into the lncRNA-mediated regulation of cardiomyocyte contractility has progressed from descriptive expression profiling to causal mechanisms supported by genetic models and direct functional measurements. Current mechanistic evidence has largely established Ca^{2+} handling and excitation-contraction coupling as major points of lncRNA regulation. *ZFAS1*, *ZNF593-AS*, and *Trdn-as* modulate distinct components of the sarcoplasmic reticulum Ca^{2+}-handling machinery[49-51], whereas MIAT influences stress-dependent Ca^{2+} cycling together with broader changes in RNA expression and splicing[45,52]. These studies demonstrate that lncRNAs can exert substantial effects on cardiac contraction by modifying the Ca^{2+} signals that initiate and terminate each contractile cycle. However, their potential contribution to the coordinated regulation of sarcomeric organization and contractile gene expression remains less well defined.

In skeletal muscle, *lnc-mg* has been reported to promote myogenic differentiation and muscle maturation through competing endogenous RNA-mediated regulation of myogenic pathways[20]. Our findings add to the current understanding of contractility-related lncRNAs by implicating *lnc-mg* in the maintenance of sarcomere- and myofibril-related gene programs in the adult heart. This observation complements the established roles of lncRNAs in Ca^{2+} handling and suggests that lncRNA-dependent regulation of cardiac contractility may also involve the molecular organization of the contractile apparatus.

This contractile role may be especially relevant after MI, when the loss of cardiac function reflects not only structural injury but also the metabolic constraints imposed on surviving myocardium[53-55]. Acute ischemic stress can compromise mitochondrial ATP generation and high-energy phosphotransfer[53]. The resulting mismatch between energy supply and mechanical demand, together with disturbances in mitochondrial Ca^{2+} handling and redox homeostasis, impairs excitation-contraction coupling and limits myocardial contractile reserve[53,56,57]. Acute metabolic stress may also influence inflammatory injury and subsequent repair; in patients with diabetes and acute MI, SGLT2 inhibitor use has been associated with a lower inflammatory burden and smaller infarct size[58]. Thus, the ability of *lnc-mg* to maintain the cardiomyocyte contractile program may be particularly relevant after MI, when the contractile capacity of surviving myocardium is additionally challenged by acute metabolic and inflammatory stress.

Dysregulated alternative splicing of sarcomeric, ion-channel, and Ca^{2+}-handling genes is increasingly recognized as an important contributor to cardiomyopathy and cardiac dysfunction[59]. Among the RBPs that govern cardiac alternative splicing, MBNL1 has emerged as an important regulator of post-transcriptional RNA processing during cardiac development and maturation. Loss of *Mbnl1* disrupts developmental splicing transitions, resulting in widespread abnormalities in transcripts involved in sarcomere organization, ion handling, and cardiac function, ultimately leading to progressive cardiac dysfunction in mice[60]. A recent study further established MBNL1 as a regulator of postnatal cardiomyocyte maturation, demonstrating that genetic ablation induces pervasive alternative splicing defects accompanied by impaired sarcomeric organization and cardiac dysfunction[61]. Against this biological background, the observed association between *lnc-mg* and MBNL1 suggests a potential connection between *lnc-mg* and post-transcriptional regulation of cardiomyocyte contractile programs.

MBNL1 preferentially recognizes structurally accessible YGCY-containing RNA sequences through its zinc-finger domains, and the YGCY motifs predicted to be exposed in *lnc-mg* may contribute to this association[39,62,63]. Protein-RNA docking has become a useful approach for generating testable structural models of RNA-protein recognition, and benchmark evaluations have demonstrated that HDOCK can recover near-native binding modes across diverse protein-RNA complexes[64-66]. Nevertheless, molecular docking relies on static structural models and computational scoring functions and therefore cannot independently establish direct physical binding or provide a definitive measure of binding affinity. In the present study, the docking results were interpreted together with the RIP enrichment and the overlap between the predicted interaction interface and structurally accessible YGCY motifs in *lnc-mg*. The convergence of these complementary findings supports the structural plausibility of the *lnc-mg*-MBNL1 association, although direct binding and the precise interaction interface remain to be experimentally established.

Notably, *lnc-mg* deficiency markedly reduced the nuclear accumulation of MBNL1. Previous studies have shown that MBNL1 nuclear localization is regulated by a bipartite nuclear localization signal comprising regions encoded by exons 5 and 6, as well as a conformation-dependent nuclear localization signal modulated by exon 7 splicing[67,68]. These findings provide a potential mechanistic framework for understanding the relationship between *lnc-mg* and MBNL1 localization. However, the present study did not directly examine the kinetics of MBNL1 nuclear import or export. Therefore, the reduced nuclear-to-cytoplasmic ratio observed following *lnc-mg* deletion could reflect impaired nuclear import, reduced nuclear retention, or increased nuclear export, and these possibilities cannot currently be distinguished. Moreover, to our knowledge, a functional nuclear export signal has not been experimentally established for MBNL1, and whether *lnc-mg* modulates MBNL1 localization through a putative NES-dependent export mechanism therefore represents an important question for future investigation. Alternatively, association with *lnc-mg* could influence the interaction of MBNL1 with other RNA or protein partners involved in its nuclear retention or nucleocytoplasmic shuttling. Further studies defining the relevant export determinants and interacting partners of MBNL1 will be required to clarify whether NES-dependent, competitive, or conformational mechanisms contribute to the altered subcellular localization of MBNL1.

Reanalysis of published cardiac MBNL1 CLIP-seq datasets showed that MBNL1-bound transcripts are predominantly enriched in biological processes related to sarcomere assembly, cardiomyocyte development, and muscle contraction[39]. Together with the observed redistribution of MBNL1 following *lnc-mg* deficiency, these findings indicate a convergence between altered MBNL1 subcellular distribution observed following *lnc-mg* deficiency and MBNL1-associated post-transcriptional programs. Further delineation of the molecular events that regulate MBNL1 trafficking will be important for determining whether and how this association contributes to downstream changes in the cardiac contractile program.

Limitations

Further investigation of the molecular determinants underlying the *lnc-mg*-MBNL1 association may provide a more detailed understanding of whether and how this association influences MBNL1 localization and activity. Although the complementary evidence from RIP, structural prediction, and subcellular localization supports a biologically relevant association between *lnc-mg* and MBNL1, the structural features that mediate their recognition remain to be defined. In particular, it will be informative to determine whether *lnc-mg* influences MBNL1 nucleocytoplasmic distribution by altering protein conformation, modulating the accessibility of its nuclear localization signals, facilitating its interaction with nuclear transport machinery, or stabilizing its association with nuclear RNA-protein assemblies. Dynamic measurements of MBNL1 trafficking, together with targeted perturbation of the predicted interaction regions, would help distinguish the relative contributions of nuclear import, nuclear retention, and nuclear export to the reduced nuclear accumulation observed following *lnc-mg* deficiency.

The downstream RNA-regulatory events connecting the *lnc-mg*-MBNL1 association to cardiomyocyte contraction also merit further investigation. The enrichment of MBNL1-associated transcripts in pathways related to sarcomere organization, cardiomyocyte development, and muscle contraction, together with the attenuation of *lnc-mg*-associated contractile effects following *Mbnl1* knockdown, provides a basis for examining how changes in MBNL1 localization are translated into functional alterations of the contractile apparatus. Integrating transcriptome-wide analyses of alternative splicing, RNA stability, and transcript localization with MBNL1 occupancy profiling may identify the specific post-transcriptional events associated with this relationship and relevant to sarcomeric and myofibrillar gene programs. Such analyses may also distinguish direct MBNL1-dependent regulatory events from broader adaptive changes in cardiomyocyte gene expression.

Several design-related considerations should be taken into account when interpreting the *in vivo* findings. Because the animal experiments were performed exclusively in male mice, whether the effects of *lnc-mg* deficiency extend to females remains to be established. With respect to the genetic control strategy, Cre-negative *lnc-mg*$^{fl/fl}$ littermates were used as controls, consistent with recent studies employing constitutive *cTnT*-Cre-mediated gene deletion in which Cre-positive floxed knockout mice were evaluated against Cre-negative floxed littermates[69,70]. This approach provided a littermate-matched reference for the floxed genetic background and is supported by established practice in cardiac conditional knockout studies. Nonetheless, the absence of a Cre-positive *lnc-mg* WT group meant that any effect attributable specifically to the *cTnT*-Cre transgene could not be examined independently. Future studies incorporating this additional genetic control and animals of both sexes would provide a more comprehensive assessment of the specificity and generalizability of the cardiac phenotype associated with *lnc-mg* deficiency.

CONCLUSION

In summary, our findings identify *lnc-mg* as a regulator of cardiomyocyte contractility and support its association with maintenance of coordinated contractile gene programs. These findings expand current understanding of RNA-mediated regulation of myocardial function and suggest that contractility-associated lncRNAs warrant further investigation as candidate therapeutic targets for MI.

DECLARATIONS

Acknowledgments

The Graphical Abstract was created with BioRender. Jia S, (2026) https://BioRender.com/2f2cips.

Authors' contributions

Conceived the study and drafted the manuscript: Jia S, Cui Y, Fan C, Bai L
Analyzed and interpreted the experimental data: Jia S, Cui Y, Bai L
Performed the experiments and collected the data: Jia S, Wu M, Bai L

Supervised the study, critically revised the manuscript, and acquired funding: Nie Y, Meng Y, Bai L
All authors contributed to the article and approved the final submitted version.

Availability of data and materials

All other data supporting the findings of this study are available from the corresponding author upon reasonable request.

AI and AI-assisted tools statement

ChatGPT (version GPT-5.5, released 2026-04-23; OpenAI) was used solely to assist with language editing and polishing of selected sections of the Introduction, Results, and Discussion. The AI tool did not contribute to the study design, data collection, data analysis, interpretation of the results, or any scientific conclusions. All authors reviewed and edited the generated text as appropriate and take full responsibility for the accuracy, integrity, and final content of the manuscript.

Financial support and sponsorship

The National Natural Science Foundation of China (Grant Nos. 82300448, 82425006, and 82570466); The National Key Research and Development Program of China (Grant No. 2022YFA1104503); The Noncommunicable Chronic Diseases-National Science and Technology Major Project (Grant No. 2023ZD0504500); The Chinese Academy of Medical Sciences (CAMS) Innovation Fund for Medical Sciences (CAMS-I2M; Grant Nos. 2024-I2M-TS-003, 2023-I2M-2-003, and 2024-I2M-C&T-B-046); The Non-profit Central Research Institute Fund of Chinese Academy of Medical Sciences (Grant Nos. 2024-RC320-04, 2024-XHQN23, and 2023-PT310-03); The National High Level Hospital Clinical Research Funding (Grant No. 2025-GSP-GG-28); The State Key Laboratory of Cardiovascular Disease (Grant No. 2025GZZD-01).

Conflicts of interest

All authors declared that there are no conflicts of interest.

Ethical approval and consent to participate

All animal experiments were approved by the Institutional Animal Care and Use Committee of Fuwai Hospital, Chinese Academy of Medical Sciences and Peking Union Medical College, and were conducted in accordance with the Guide for the Care and Use of Laboratory Animals and institutional guidelines (approval no. 0108-7-2200-ZX).

Consent for publication

Not applicable.

Supplementary Materials

Supplementary Materials

REFERENCES

1. Mensah GA, Fuster V, Murray CJ, et al. Global burden of cardiovascular diseases and risks, 1990-2022. *J Am Coll Cardiol.* 2023;82:2350-473. DOI PubMed
2. Stark BA, Decleene NK, Desai EC, et al. Global, regional, and national burden of cardiovascular diseases and risk factors in 204 countries and territories, 1990-2023. *J Am Coll Cardiol.* 2025;86:2167-243. DOI PubMed
3. Byrne RA, Rossello X, Coughlan JJ, et al. 2023 ESC guidelines for the management of acute coronary syndromes. *Eur Heart J.* 2023;44:3720-826. DOI PubMed
4. Heusch G. Myocardial ischemia/reperfusion: Translational pathophysiology of ischemic heart disease. *Med.* 2024;5:10-31. DOI PubMed
5. Frantz S, Hundertmark MJ, Schulz-Menger J, Bengel FM, Bauersachs J. Left ventricular remodelling post-myocardial infarction: pathophysiology, imaging, and novel therapies. *Eur Heart J.* 2022;43:2549-61. DOI PubMed PMC
6. Heusch G. Coronary blood flow in heart failure: cause, consequence and bystander. *Basic Res Cardiol.* 2022;117:1. DOI PubMed PMC

7. Dauw J, Martens P, Deferm S, et al. Left ventricular function recovery after ST-elevation myocardial infarction: correlates and outcomes. *Clin Res Cardiol.* 2021;110:1504-15. DOI
8. Yu X, Chen X, Amrute-Nayak M, et al. MARK4 controls ischaemic heart failure through microtubule detyrosination. *Nature.* 2021;594:560-5. DOI PubMed PMC
9. Yu S, Sun Z, Wang X, et al. Mettl13 protects against cardiac contractile dysfunction by negatively regulating C-Cbl-mediated ubiquitination of SERCA2a in ischemic heart failure. *Sci China Life Sci.* 2023;66:2786-804. DOI
10. Chen Y, Liu S, Liang Y, et al. Single dose of intravenous miR199a-5p delivery targeting ischemic heart for long-term repair of myocardial infarction. *Nat Commun.* 2024;15:5565. DOI PubMed PMC
11. Ferrer J, Dimitrova N. Transcription regulation by long non-coding RNAs: mechanisms and disease relevance. *Nat Rev Mol Cell Biol.* 2024;25:396-415. DOI PubMed PMC
12. Mattick JS, Amaral PP, Carninci P, et al. Long non-coding RNAs: definitions, functions, challenges and recommendations. *Nat Rev Mol Cell Biol.* 2023;24:430-47. DOI PubMed PMC
13. Han P, Li W, Lin C, et al. A long noncoding RNA protects the heart from pathological hypertrophy. *Nature.* 2014;514:102-6. DOI PubMed PMC
14. Du H, Zhao Y, Wen J, et al. LncRNA DCRT protects against dilated cardiomyopathy by preventing NDUFS2 alternative splicing by binding to PTBP1. *Circulation.* 2024;150:1030-49. DOI
15. Zhang Y, Zhang X, Cai B, et al. The long noncoding RNA lncCIRBIL disrupts the nuclear translocation of Bclaf1 alleviating cardiac ischemia-reperfusion injury. *Nat Commun.* 2021;12:522. DOI PubMed PMC
16. Gao R, Wang L, Bei Y, et al. Long noncoding RNA cardiac physiological hypertrophy-associated regulator induces cardiac physiological hypertrophy and promotes functional recovery after myocardial ischemia-reperfusion injury. *Circulation.* 2021;144:303-17. DOI
17. Liu N, Kataoka M, Wang Y, et al. LncRNA LncHrt preserves cardiac metabolic homeostasis and heart function by modulating the LKB1-AMPK signaling pathway. *Basic Res Cardiol.* 2021;116:48. DOI PubMed PMC
18. Rogala S, Ali T, Melissari M, et al. The lncRNA sweetheart regulates compensatory cardiac hypertrophy after myocardial injury in murine males. *Nat Commun.* 2023;14:7024. DOI PubMed PMC
19. Yang H, Xuan L, Wang S, et al. LncRNA CCRR maintains Ca^{2+} homeostasis against myocardial infarction through the FTO-SERCA2a pathway. *Sci China Life Sci.* 2024;67:1601-19. DOI
20. Zhu M, Liu J, Xiao J, et al. *Lnc-mg* is a long non-coding RNA that promotes myogenesis. *Nat Commun.* 2017;8:14718. DOI PubMed PMC
21. Pinheiro A, Naya FJ. The Key Lnc (RNA)s in cardiac and skeletal muscle development, regeneration, and disease. *J Cardiovasc Dev Dis.* 2021;8:84. DOI PubMed PMC
22. Sweta S, Dudnakova T, Sudheer S, Baker AH, Bhushan R. Importance of long non-coding RNAs in the development and disease of skeletal muscle and cardiovascular lineages. *Front Cell Dev Biol.* 2019;7:228. DOI PubMed PMC
23. Martone J, Mariani D, Desideri F, Ballarino M. Non-coding RNAs shaping muscle. *Front Cell Dev Biol.* 2020;7:394. DOI PubMed PMC
24. Jiao K, Kulessa H, Tompkins K, et al. An essential role of Bmp4 in the atrioventricular septation of the mouse heart. *Genes Dev.* 2003;17:2362-7. DOI PubMed PMC
25. Faul F, Erdfelder E, Lang A, Buchner A. G*Power 3: a flexible statistical power analysis program for the social, behavioral, and biomedical sciences. *Behav Res Methods.* 2007;39:175-91. DOI PubMed
26. Deng Y, Xie M, Li Q, et al. Targeting mitochondria-inflammation circuit by β-hydroxybutyrate mitigates HFpEF. *Circ Res.* 2021;128:232-45. DOI
27. Abelanet A, Camoin M, Rubin S, et al. Increased capillary permeability in heart induces diastolic dysfunction independently of inflammation, fibrosis, or cardiomyocyte dysfunction. *Arterioscler Thromb Vasc Biol.* 2022;42:745-63. DOI PubMed
28. Lian H, Qin Z, Wu M, et al. Contractility detection of isolated mouse papillary muscle using myotronic Myostation-Intact device. *Anim Models Exp Med.* 2022;5:445-52. DOI PubMed PMC
29. Powers JD, Kirkland NJ, Liu C, et al. Subcellular remodeling in filamin C deficient mouse hearts impairs myocyte tension development during progression of dilated cardiomyopathy. *Int J Mol Sci.* 2022;23:871. DOI PubMed PMC
30. Gan P, Wang Z, Bezprozvannaya S, et al. RBPMS regulates cardiomyocyte contraction and cardiac function through RNA alternative splicing. *Cardiovasc Res.* 2024;120:56-68. DOI PubMed PMC
31. Yamaguchi N, Xiao J, Narke D, et al. Cardiac pressure overload decreases ETV1 expression in the left atrium, contributing to atrial electrical and structural remodeling. *Circulation.* 2021;143:805-20. DOI PubMed
32. Li Y, Dong M, Wang Q, et al. HIMF deletion ameliorates acute myocardial ischemic injury by promoting macrophage transformation to reparative subtype. *Basic Res Cardiol.* 2021;116:30. DOI PubMed PMC

33. Takagawa J, Zhang Y, Wong ML, et al. Myocardial infarct size measurement in the mouse chronic infarction model: comparison of area- and length-based approaches. *J Appl Physiol.* 2007;102:2104-11. DOI PubMed PMC
34. Brito-Estrada O, Kuwabara Y, Gibson AM, et al. DWORF gene therapy improves cardiac calcium handling and mitochondrial function. *Circ Res.* 2025;137:1072-88. DOI PubMed PMC
35. Love MI, Huber W, Anders S. Moderated estimation of fold change and dispersion for RNA-seq data with DESeq2. *Genome Biol.* 2014;15:550. DOI PubMed PMC
36. Zhou K, Huang J, Liu S, et al. An encyclopedic regulatory and functional atlas of RNA interactomes. *Nat Methods.* 2026;23:1109-14. DOI PubMed
37. Kang J, Tang Q, He J, et al. RNAInter v4.0: RNA interactome repository with redefined confidence scoring system and improved accessibility. *Nucleic Acids Res.* 2022;50:D326-32. DOI PubMed PMC
38. Muppirala UK, Honavar VG, Dobbs D. Predicting RNA-protein interactions using only sequence information. *BMC Bioinformatics.* 2011;12:489. DOI PubMed PMC
39. Wang ET, Cody NA, Jog S, et al. Transcriptome-wide regulation of pre-mRNA splicing and mRNA localization by muscleblind proteins. *Cell.* 2012;150:710-24. DOI PubMed PMC
40. Lv C, Alimu X, Xiao X, et al. Somatic NAP1L1 p.D349E promotes cardiac hypertrophy through cGAS-STING-IFN signaling. *Nat Commun.* 2025;16:3140. DOI PubMed PMC
41. Maguy A, Tessier A, Mahendran Y, et al. Anti-TRPV2 autoantibody linked to sudden infant death syndrome. *Circulation.* 2025;152:81-4. DOI PubMed
42. Fan J, Li Z, Lin L, et al. The potential value of long non-coding RNA in molecular diagnosis and forensic identification of heart failure. *Vessel Plus.* 2026;10:22. DOI
43. Wang J, Chen X, Shen D, et al. A long noncoding RNA NR_045363 controls cardiomyocyte proliferation and cardiac repair. *J Mol Cell Cardiol.* 2019;127:105-14. DOI PubMed
44. Ponnusamy M, Liu F, Zhang Y, et al. Long noncoding RNA CPR (cardiomyocyte proliferation regulator) regulates cardiomyocyte proliferation and cardiac repair. *Circulation.* 2019;139:2668-84. DOI
45. Bai X, Yang C, Jiao L, et al. LncRNA MIAT impairs cardiac contractile function by acting on mitochondrial translocator protein TSPO in a mouse model of myocardial infarction. *Sig Transduct Target Ther.* 2021;6:172. DOI PubMed PMC
46. Ma T, Qiu F, Gong Y, et al. Therapeutic silencing of lncRNA RMST alleviates cardiac fibrosis and improves heart function after myocardial infarction in mice and swine. *Theranostics.* 2023;13:3826-43. DOI PubMed PMC
47. Shumliakivska M, Fischer A, Muhly-Reinholz M, et al. The long non-coding RNA Snhg15 protects the heart after myocardial infarction. *J Mol Cell Cardiol.* 2026;210:72-82. DOI
48. Liang X, Liu S, Liu G, et al. LncRNA SNHG15 promotes angiogenesis and improves cardiac repair after myocardial infarction through MiR-665-mediated KDR expression. *Cell Mol Life Sci.* 2025;82:211. DOI PubMed PMC
49. Zhang Y, Jiao L, Sun L, et al. LncRNA*ZFAS1* as a SERCA2a inhibitor to cause intracellular Ca^{2+} overload and contractile dysfunction in a mouse model of myocardial infarction. *Circ Res.* 2018;122:1354-68. DOI PubMed PMC
50. Fan J, Li H, Xie R, et al. LncRNA ZNF593-AS alleviates contractile dysfunction in dilated cardiomyopathy. *Circ Res.* 2021;128:1708-23. DOI
51. Zhao Y, Riching AS, Knight WE, et al. Cardiomyocyte-specific long noncoding RNA regulates alternative splicing of the triadin gene in the heart. *Circulation.* 2022;146:699-714. DOI PubMed
52. Yang L, Deng J, Ma W, et al. Ablation of lncRNA *Miat* attenuates pathological hypertrophy and heart failure. *Theranostics.* 2021;11:7995-8007. DOI PubMed PMC
53. Aksentijevic D, Sedej S, Fauconnier J, et al. Mechano-energetic uncoupling in heart failure. *Nat Rev Cardiol.* 2025;22:773-97. DOI
54. Bornstein MR, Tian R, Arany Z. Human cardiac metabolism. *Cell Metab.* 2024;36:1456-81. DOI PubMed PMC
55. Lygate CA. Maintaining energy provision in the heart: the creatine kinase system in ischaemia-reperfusion injury and chronic heart failure. *Clin Sci.* 2024;138:491-514. DOI PubMed PMC
56. Ritterhoff J, Tian R. Metabolic mechanisms in physiological and pathological cardiac hypertrophy: new paradigms and challenges. *Nat Rev Cardiol.* 2023;20:812-29. DOI PubMed
57. Lopaschuk GD, Karwi QG, Tian R, Wende AR, Abel ED. Cardiac energy metabolism in heart failure. *Circ Res.* 2021;128:1487-513. DOI PubMed PMC
58. Paolisso P, Bergamaschi L, Santulli G, et al. Infarct size, inflammatory burden, and admission hyperglycemia in diabetic patients with acute myocardial infarction treated with SGLT2-inhibitors: a multicenter international registry. *Cardiovasc Diabetol.* 2022;21:77. DOI PubMed PMC
59. Cao J, Wei Z, Nie Y, Chen H. Therapeutic potential of alternative splicing in cardiovascular diseases. *eBioMedicine.* 2024;101:104995. DOI PubMed PMC

60. Dixon DM, Choi J, El-Ghazali A, et al. Loss of muscleblind-like 1 results in cardiac pathology and persistence of embryonic splice isoforms. *Sci Rep.* 2015;5:9042. DOI PubMed PMC
61. Bailey LR, Bugg D, Reichardt IM, et al. MBNL1 regulates programmed postnatal switching between regenerative and differentiated cardiac states. *Circulation.* 2024;149:1812-29. DOI PubMed PMC
62. Goers ES, Purcell J, Voelker RB, Gates DP, Berglund JA. MBNL1 binds GC motifs embedded in pyrimidines to regulate alternative splicing. *Nucleic Acids Res.* 2010;38:2467-84. DOI PubMed PMC
63. Teplova M, Patel DJ. Structural insights into RNA recognition by the alternative-splicing regulator muscleblind-like MBNL1. *Nat Struct Mol Biol.* 2008;15:1343-51. DOI PubMed PMC
64. Yan Y, Zhang D, Zhou P, Li B, Huang S. HDOCK: a web server for protein-protein and protein-DNA/RNA docking based on a hybrid strategy. *Nucleic Acids Res.* 2017;45:W365-73. DOI PubMed PMC
65. Huang SY, Zou X. A nonredundant structure dataset for benchmarking protein-RNA computational docking. *J Comput Chem.* 2012;34:311-8. DOI PubMed PMC
66. Nithin C, Mukherjee S, Bahadur RP. A non-redundant protein-RNA docking benchmark version 2.0. *Proteins Struct Funct Bioinf.* 2017;85:256-67. DOI
67. Tran H, Gourrier N, Lemercier-Neuillet C, et al. Analysis of exonic regions involved in nuclear localization, splicing activity, and dimerization of muscleblind-like-1 isoforms. *J Biol Chem.* 2011;286:16435-46. DOI PubMed PMC
68. Kino Y, Washizu C, Kurosawa M, et al. Nuclear localization of MBNL1: splicing-mediated autoregulation and repression of repeat-derived aberrant proteins. *Hum Mol Genet.* 2015;24:740-56. DOI
69. Gao F, Liang T, Lu YW, et al. A defect in mitochondrial protein translation influences mitonuclear communication in the heart. *Nat Commun.* 2023;14:1595. DOI PubMed PMC
70. Lu YW, Liang Z, Dorr K, et al. PCBP1 regulates alternative splicing of AARS2 in congenital cardiomyopathy. *Nat Cardiovasc Res.* 2026;5:328-50. DOI PubMed PMC